UC San Diego

UC San Diego Previously Published Works

Title

Polaritonic Probe of an Emergent 2D Dipole Interface

Permalink

https://escholarship.org/uc/item/248338d0

Journal

Nano Letters, 23(18)

ISSN

1530-6984

Authors

Rizzo, Daniel J
Zhang, Jin
Jessen, Bjarke S
et al.

Publication Date

2023-09-27

DOI

10.1021/acs.nanolett.3c01611

Copyright Information

This work is made available under the terms of a Creative Commons Attribution License, availalbe at https://creativecommons.org/licenses/by/4.0/

Peer reviewed

eScholarship.org Powered by the California Digital Library
University of California

NANO LETTERS

pubs.acs.org/NanoLett Letter

Polaritonic Probe of an Emergent 2D Dipole Interface

Daniel J. Rizzo,*[,&] Jin Zhang,[&] Bjarke S. Jessen, Francesco L. Ruta, Matthew Cothrine, Jiaqiang Yan, David G. Mandrus, Stephen E. Nagler, Takashi Taniguchi, Kenji Watanabe, Michael M. Fogler, Abhay N. Pasupathy, Andrew J. Millis, Angel Rubio,* James C. Hone, Cory R. Dean,* and D. N. Basov*

Cite This: https://doi.org/10.1021/acs.nanolett.3c01611 Read Online

ACCESS | Metrics & More | Article Recommendations | Supporting Information

ABSTRACT: The use of work-function-mediated charge transfer has recently emerged as a reliable route toward nanoscale electrostatic control of individual atomic layers. Using α-$RuCl_3$ as a 2D electron acceptor, we are able to induce emergent nano-optical behavior in hexagonal boron nitride (*h*BN) that arises due to interlayer charge polarization. Using scattering-type scanning near-field optical microscopy (s-SNOM), we find that a thin layer of α-$RuCl_3$ adjacent to an *h*BN slab reduces the propagation length of *h*BN phonon polaritons (PhPs) in significant excess of what can be attributed to intrinsic optical losses. Concomitant nano-optical spectroscopy experiments reveal a novel resonance that aligns energetically with the region of excess PhP losses. These experimental observations are elucidated by first-principles density-functional theory and near-field model calculations, which show that the formation of a large interfacial dipole suppresses out-of-plane PhP propagation. Our results demonstrate the potential utility of charge-transfer heterostructures for tailoring optoelectronic properties of 2D insulators.

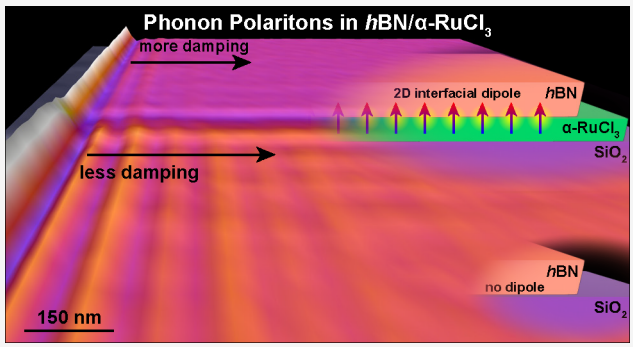

KEYWORDS: *phonon polaritons, charge transfer, α-$RuCl_3$, scanning near-field optical microscopy (SNOM), two-dimensional (2D) materials, heterostructures*

Two-dimensional (2D) van der Waals (vdW) compounds are highly tunable, atomically thin crystals that are ideal platforms for studying fundamental phenomena in quantum materials. Recent advances in synthesis and fabrication techniques have spawned a panoply of 2D layers that display a wide range of physical behaviors, including magnetism,[1−9] topology,[10−16] electron correlations,[17−22] and superconductivity.[12,22−28] Among 2D materials, hexagonal boron nitride (*h*BN) has emerged as a ubiquitous 2D insulator, possessing a band gap of roughly 6 eV[29,30] and often acting as a de facto protective encapsulating layer in 2D devices.[31,32] On the other hand, *h*BN is not exclusively relegated to the role of passive adlayer. For instance, charge defects in *h*BN can be engineered to generate quantum dots in graphene,[33−37] and twisted *h*BN bilayers have been shown to display emergent ferroelectric behavior.[38,39] Furthermore, *h*BN is a robust platform for supporting propagating mid-infrared (MIR) phonon polaritons (PhPs) and has been heavily studied as a medium for hosting nanostructured light.[40−51] Previous studies have shown that the behavior of PhPs in *h*BN can be engineered by tuning layer thickness,[40,42,43] varying isotopic ratios,[41,44] patterning with nanolithographic etching,[48,51] and proximitizing to graphene.[45−47] Here, we harness PhPs hosted by *h*BN to act as reporters of the emergent optoelectronic properties at *h*BN/α-$RuCl_3$ interfaces, a task that is difficult to accomplish with alternative experimental approaches.

Beyond the engineering of single 2D layers, novel properties can be accessed through the creation of 2D heterostructures, where two or more atomic layers are combined to realize emergent physical behavior not attainable in the isolated form of the constituent materials. These include correlated behavior in twisted moiré multilayer systems,[18,19,21,22] interlayer excitons,[52−55] proximate magnetism,[56,57] and 2D charge-transfer doping.[57−67] In the case of charge-transfer doping, recent work[57−64] has focused on the use of α-$RuCl_3$—a high-work-function 2D insulator capable of generating heavily doped 2D materials through interfacial charge transfer. In heterostructures with graphene, work-function-mediated interlayer charge transfer with α-$RuCl_3$ results in a hole density in excess of 10^{13} cm^{-2}. This carrier density can be further tuned through increased layer separation[59] or the introduction of

Received: April 28, 2023
Revised: July 14, 2023
Published: July 26, 2023

ACS Publications © 2023 American Chemical Society

interstitial layers.[60,61] The atomically sharp interfacial dipole in graphene/α-$RuCl_3$ heterostructures also permits nanometer-scale lateral heterojunctions,[59,61] which show novel transport behavior[61] and prompt abrupt changes in the local conductivity revealed by plasmonic scattering.[58,59] In principle, α-$RuCl_3$ can be interfaced with a wide range of 2D materials[68] to generate strong interfacial dipoles. For instance, a recent theoretical prediction[64] states that a similarly high interfacial charge transfer should occur in *h*BN/α-$RuCl_3$ heterostructures. However, it is not clear from these predictions how such a large work function difference should impact the properties of *h*BN/α-$RuCl_3$, with each component being bulk insulators lacking free carriers in their native state.

In this study, we use scattering-type scanning near-field optical microscopy (s-SNOM) in conjunction with density functional theory (DFT) to unravel the charge transfer hypothesis applied to *h*BN/α-$RuCl_3$ heterostructures. We find that the presence of few-layer α-$RuCl_3$ at the 2D interface with *h*BN significantly reduces the propagation length of PhPs compared to *h*BN supported directly by a SiO_2 substrate. This experimental observation is contrary to modeling results based on the intrinsic optical properties of α-$RuCl_3$ and SiO_2, since the prior is expected to be a less lossy substrate in the MIR frequency range. In addition, colocated nano-optical spectroscopy displays a novel resonance at similar MIR energies that is not expected to exist. DFT calculations reveal a likely source of these anomalous results, as the difference between the *h*BN/α-$RuCl_3$ work functions (ΔW = ~2 eV)[69,70] gives rise to a large out-of-plane dipole that is not otherwise accounted for in standard nano-optical modeling. We find that the propagation of PhPs is maximally suppressed when aligned to the adjacent dipole layer, giving rise to excess losses and emergent nano-optical contrast. Our study validates the notion of charge polarization at the *h*BN/α-$RuCl_3$ interface and demonstrates that interfacial doping with α-$RuCl_3$ can be used with wide band gap insulators to generate novel behavior in 2D confined light.

RESULTS AND DISCUSSION

In order to fabricate *h*BN/α-$RuCl_3$ heterostructures, individual layers of *h*BN and α-$RuCl_3$ were first isolated on SiO_2/Si chips following established exfoliation procedures. Crystals of *h*BN with a nominal thickness of 20 nm were lifted with a polycarbonate (PC) coated transfer slide and partially deposited on a few-layer α-$RuCl_3$ crystal. The resulting stack consists of regions of *h*BN in direct contact with the underlying SiO_2 substrate and regions with interstitial few-layer α-$RuCl_3$ (see Methods and Figure S1 for detailed procedure). A schematic representation of the resulting 2D heterostructure is shown in Figure 1A along with a topographic image collected with atomic force microscopy (AFM; Figure 1B). Electrostatic reasoning based on the difference between the work function of α-$RuCl_3$ (W = 6.1 eV)[69] and *h*BN (W = ~4.1 eV)[70] suggests that the fabrication of this interface should promote the formation of an interfacial dipole with a nontrivial component aligned with the PhP propagation direction (Figure 1A). First-principles DFT calculations validate this intuition, showing a Bader charge transfer of 0.9×10^{13} cm^{-2} at the interface of a model monolayer-on-monolayer system (Figures 1C). Given a 3.3 Å interatomic distance between layers, this corresponds to a 2D polarization density of $\sim 3.0 \times 10^5$ e cm^{-1}.

Next, we harnessed the phonon polaritons of *h*BN to explore the dynamics associated with interfacial dipoles in *h*BN/α-$RuCl_3$ structures. Since the wavelength of PhPs is in excess of 200 nm, the field of PhP waves can be employed to interrogate properties of proximal layers along with emergent responses at interfaces. Specifically, we performed a series of experiments using s-SNOM to visualize PhPs in both the *h*BN/α-$RuCl_3$/SiO_2 and *h*BN/SiO_2 regions of our devices (Figure 2). Here, the near-field amplitude (S_n) and phase (Φ_n) are demodulated at the nth harmonic ($n \geq 4$) of the tip-tapping frequency to minimize far-field contributions to the detected signal (see Methods). Figure 2A shows a characteristic map of the near-field amplitude for the device in Figure 1B collected with an incident laser frequency of ω = 1494.5 cm^{-1}. The appearance of periodic modulations in the near-field amplitude (herein referred to as "fringes") is a hallmark of PhPs. Polaritonic fringes are observed in regions of *h*BN both with and without

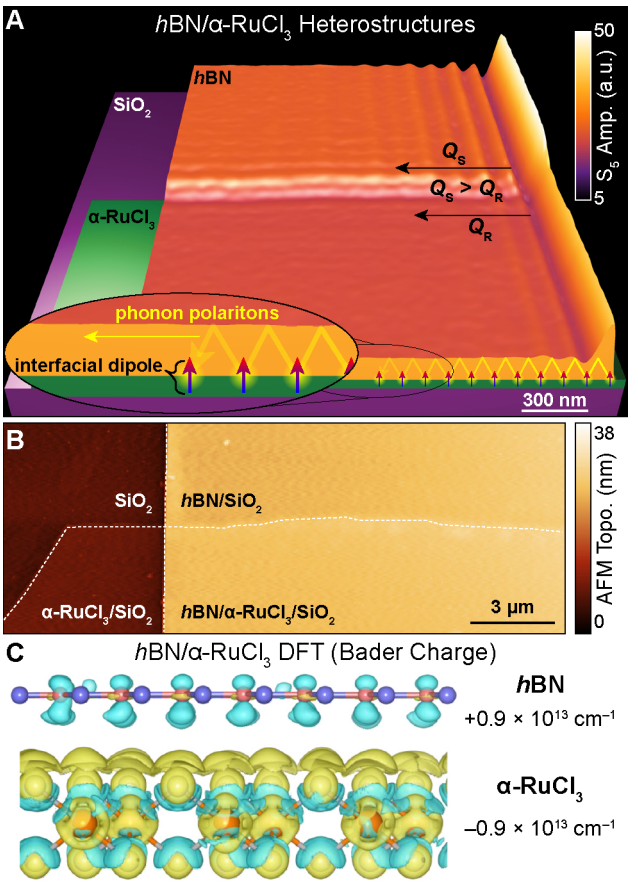

Figure 1. Overview of charge redistribution and s-SNOM measurements on *h*BN/α-$RuCl_3$ heterostructures. (A) Schematic overview of *h*BN/α-$RuCl_3$ heterostructures overlaid with experimental s-SNOM measurements of PhPs (S_5 amplitude, ω = 1494.5 cm^{-1}). A dipole develops at the *h*BN/α-$RuCl_3$ interface due to the difference in work function between the two materials. PhPs propagating in *h*BN/α-$RuCl_3$/SiO_2 are significantly damped compared to PhPs in the region directly on SiO_2 as seen by the difference in their Q factors (i.e., $Q_S > Q_R$). (B) AFM topographic overview of the device showing schematically in panel A. A 22-nm-thick microcrystal of *h*BN is partially draped on 2.4 nm of α-$RuCl_3$ on a SiO_2 substrate. (C) Bader charge analysis of model *h*BN/α-$RuCl_3$ system showing interfacial charge transfer of 0.9×10^{13} cm^{-2} at the 2D interface. Iso-surfaces of constant charge difference are plotted in cyan (negative) and yellow (positive) relative to the charge density of isolated *h*BN and α-$RuCl_3$ layers. The distortion of orbitals near the interface creates a net positive charge in the *h*BN layer and a net negative charge in the α-$RuCl_3$ layer.

https://doi.org/10.1021/acs.nanolett.3c01611
Nano Lett. XXXX, XXX, XXX−XXX

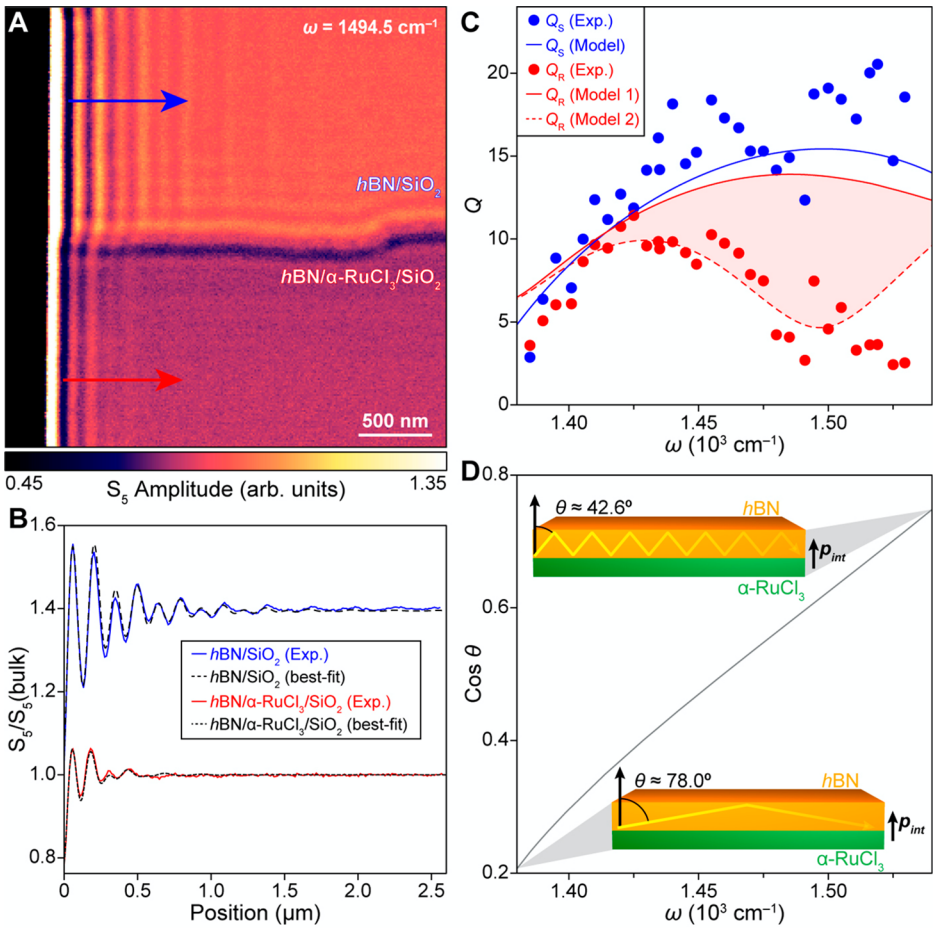

Figure 2. Phonon polariton losses for hBN/α-$RuCl_3$/SiO_2 versus hBN/SiO_2. (A) Characteristic s-SNOM image of the device shown in Figure 1B showing the S_5 amplitude collected with an incident laser frequency of ω = 1494.5 cm^{-1}. Oscillations in the S_5 amplitude emanating from the hBN edge (i.e., fringes) arise due to interference between left-moving tip-launched and right-moving edge-reflected PhPs. The region with the thin α-$RuCl_3$ layer (red arrow) has visibly fewer fringes than the region without the α-$RuCl_3$ layer (blue arrow). (B) Spatially averaged line profile of the PhP fringes in the region with (red line) and without (blue line) an underlying α-$RuCl_3$ layer (added offset of 0.4 between each curve for clarity). The dotted black lines are the best-fit model line profile used to extract the complex wavevector $\mathbf{q}$ using the method employed in refs 58 and 71 (see Figure S2). (C) The experimental frequency dependence of Q_S and Q_R is plotted with solid blue and red circles, respectively, along with their calculated values (solid blue and red lines, respectively; see Methods and Supplementary Discussion). The dashed red line shows the expected value of Q_R when α-$RuCl_3$ is modeled with emergent interfacial losses (model 2 in Figure 3), showing much better agreement with the experimental data. The shaded red region shows the change in Q_R induced by emergent interfacial losses. (D) The theoretical frequency dependence of the PhP angle of propagation θ relative to the surface normal. The component of the PhP propagation that is parallel to the hBN/α-$RuCl_3$ interfacial dipole (p_{int}) is largest over the range of frequencies at which excess PhP losses are observed in panel C.

the underlying α-$RuCl_3$. When the line profiles of the near-field amplitude in these two regions of the sample are compared (Figure 2B), it is clear that the spacing between fringes (i.e., the PhP wavelength) is only subtly affected by the presence of a very thin layer of α-$RuCl_3$. On the other hand, the underlying α-$RuCl_3$ appears to have a significant impact on the number of observable fringes (i.e., the propagation length). Specifically, the hBN/α-$RuCl_3$/SiO_2 region only shows roughly half as many fringes as the hBN/SiO_2 region for the selected frequency in Figure 2B (ω = 1494.5 cm^{-1}).

In order to gain quantitative insight into the influence of α-$RuCl_3$ on PhPs, we imaged our device over a broad range of frequencies and extracted the area-average line profiles in a manner similar to that shown in Figure 2B (Figure S2). From these images, we obtained quantitative information about the complex-valued wavevector of PhPs at the hBN/α-$RuCl_3$ interface:

$$\mathbf{q} = q_1 + iq_2 \quad (1)$$

where q_1 and q_2 are the real and imaginary components of $\mathbf{q}$, respectively. Here, q_1 quantifies the PhP confinement ($q_1 \propto 1/\lambda_p$, where λ_p is the PhP wavelength), and q_2 is inversely proportional to the PhP decay length. The ratio of these quantities ($Q = q_1/q_2$) is often used as a measure of the PhP losses and is sensitive to the intrinsic properties of hBN and the local dielectric environment. We are able to quantitatively extract $\mathbf{q}$ for PhPs visualized at all frequencies in Figure S2 by fitting a functional ansatz to the average experimental near-field profile following a similar procedure established in previous s-SNOM studies of confined light.[58,71]

The frequency dependence of q_1 (i.e., the PhP dispersions) for regions with and without α-$RuCl_3$ is shown in Figure S2C. It is apparent from this plot that α-$RuCl_3$ has a minimal influence on the PhP dispersion across a wide range of frequencies but does appear to increase the value of q_1 at high frequencies. Since the real part of the permittivity (ϵ_1) of α-$RuCl_3$ is larger than that of SiO_2 at these frequencies ($\epsilon_1^{\alpha\text{-RuCl3}} = 6.3$[72] versus $\epsilon_1^{SiO2} = 1.1$[73]), it may be expected that PhPs

https://doi.org/10.1021/acs.nanolett.3c01611
Nano Lett. XXXX, XXX, XXX−XXX

propagating on an α-$RuCl_3$ substrate become more confined than those on an SiO_2 substrate. However, this additional confinement should not be significant since our device only possesses 2.4 nm of α-$RuCl_3$. This intuition bears out when calculating the theoretical PhP dispersion from maxima in the imaginary component of the p-polarized reflection coefficient, $\mathrm{Im}[r_p]$ (using previously reported optical parameters[72−74] for the constituents of our multilayer vdW device). We find that the experimental PhP dispersion for hBN/SiO_2 matches well with this model (blue solid line in Figure S2C), while the corresponding prediction for PhPs in hBN/α-$RuCl_3$/SiO_2 somewhat underestimates the degree of experimental confinement at higher frequencies. Hypothetically, a thicker layer of α-$RuCl_3$ could provide much more substantial dielectric confinement (Figure S3A). The agreement between the experimental and theoretical dispersions indicates that the native optical parameters for hBN and α-$RuCl_3$ deviate only slightly from the gross features of our experiment. Therefore, the presence of charge polarization at hBN/α-$RuCl_3$ appears to only subtly influence the PhP dispersion.

We continue our analysis by extracting the value of Q for both regions of the sample (Q_S for hBN/SiO_2 and Q_R for hBN/α-$RuCl_3$/SiO_2). Heuristically, Q is roughly twice the number of fringes that can be observed in near-field images. One would therefore infer that $Q_S > Q_R$ based on a cursory inspection of the images of these two regions in Figure 2A. Quantitative extraction of Q_S and Q_R confirms this inference for essentially all frequencies measured in our experiment, with Q_S growing to more than 6 times the magnitude of Q_R at ω = 1530 cm^{-1} (Figure 2C). Hence, polaritons in hBN experience significant additional frequency-dependent losses as a result of the underlying 2.4 nm layer of α-$RuCl_3$. Since both SiO_2 and α-$RuCl_3$ possess potential loss channels in the MIR that can contribute to PhP damping,[72,73] it is not immediately obvious whether or not the excess PhP losses observed on α-$RuCl_3$ are consistent with expectation. In addition, the PhP Q-factor does not have a trivial dependence on the complex valued permittivity of the underlying substrate, demanding explicit calculation of the Q factors using numerical approaches in conjunction with reported optical parameters (see SI).[72−74] Contrary to our experimental results, we find that the calculated value of Q actually increases by more than a factor of 1.5 when the underlying SiO_2 substrate is replaced with a thick slab of α-$RuCl_3$ (Figure S3), indicating that α-$RuCl_3$ is a less lossy substrate than SiO_2 in this frequency range. In the case of a thin layer of α-$RuCl_3$ on SiO_2, calculation of Q_S and Q_R shows a subtle reduction in Q_R compared with Q_S (red and blue curves in Figure 2D, respectively). This is likely due to thin film effects (Figure S3B) that nevertheless fail to capture the significant frequency-dependent reduction in Q_R compared to Q_S observed in the experiment.

Informed by DFT calculations (Figure 1C), we consider how an interfacial dipole layer affects the behavior of PhPs beyond what is captured in our minimal model. In particular, PhP propagation is expected to be suppressed along the axis parallel to the interfacial dipole moment. Thus, the energy dependence of the PhP propagation angle θ relative to the surface normal provides a metric for the dipole-induced PhP damping. Given that hBN is an anisotropic medium, θ is given by

$$\theta = \tan^{-1}\sqrt{\frac{\epsilon_1^{\parallel}}{\epsilon_1^{\perp}}} \tag{2}$$

where $\epsilon_1^{\parallel}$ and $\epsilon_1^{\perp}$ are the in-plane and out-of-plane components of the real part of the hBN permittivity, respectively.[49,75] Figure 2D shows a plot of cos θ for frequencies probed experimentally in Figure 2C. At the lowest frequencies, PhPs travel nearly horizontally with θ = 78.0°. However, at higher frequencies, PhPs develop a significant out-of-plane component (θ = 42.6°), with an increase in the normalized projection along the dipole direction from 0.21 to 0.74. Thus, the frequency regime at which excess PhP losses are observed is coincident with those at which propagation becomes most aligned to the interfacial dipole.

To empirically quantify the influence of the dipole layer on PhP losses, we performed nano-optical spectroscopy by collecting a series of images on an hBN/α-$RuCl_3$ heterostructure spanning frequencies below and above those at which PhPs could be spatially resolved (Figure 3). It is apparent that, at certain frequencies (e.g., 1528 cm^{-1}), significant contrast exists in both the near-field amplitude (S_4) and phase (Φ_4) between the hBN/α-$RuCl_3$/SiO_2 and hBN/SiO_2 regions

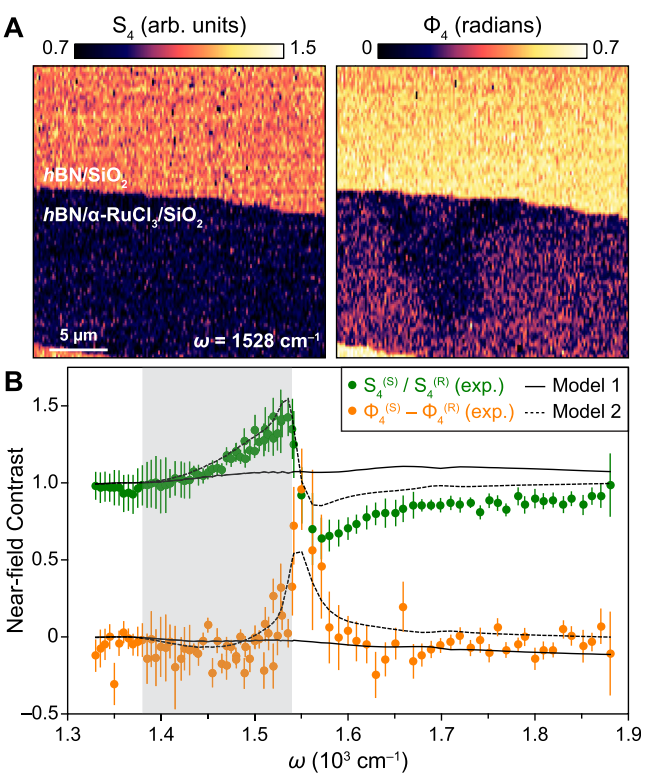

Figure 3. Nano-optical spectroscopy of hBN/α-$RuCl_3$ heterostructures. (A) The near-field S_4 amplitude (left panel) and Φ_4 phase (right panel) measured with an incident laser frequency of ω = 1528 cm^{-1} showing contrast between hBN/α-$RuCl_3$/SiO_2 and hBN/SiO_2 in both channels. (B) Nano-optical spectroscopy showing contrast in the near-field amplitude (solid green circles) and phase (solid orange circles; labeled $S_4^{(R)}$ and $\Phi_4^{(R)}$ for hBN/α-$RuCl_3$/SiO_2, and $S_4^{(S)}$ and $\Phi_4^{(S)}$ for hBN/SiO_2). The lightning rod model[76] for this spectrum is shown based on reported optical parameters (model 1, solid line) and with the addition of a fitted Lorentzian oscillator (model 2, dashed line). The latter model better captures the experimental data. The region over which PhPs are observed to have excess losses is highlighted in gray.

https://doi.org/10.1021/acs.nanolett.3c01611
Nano Lett. XXXX, XXX, XXX−XXX

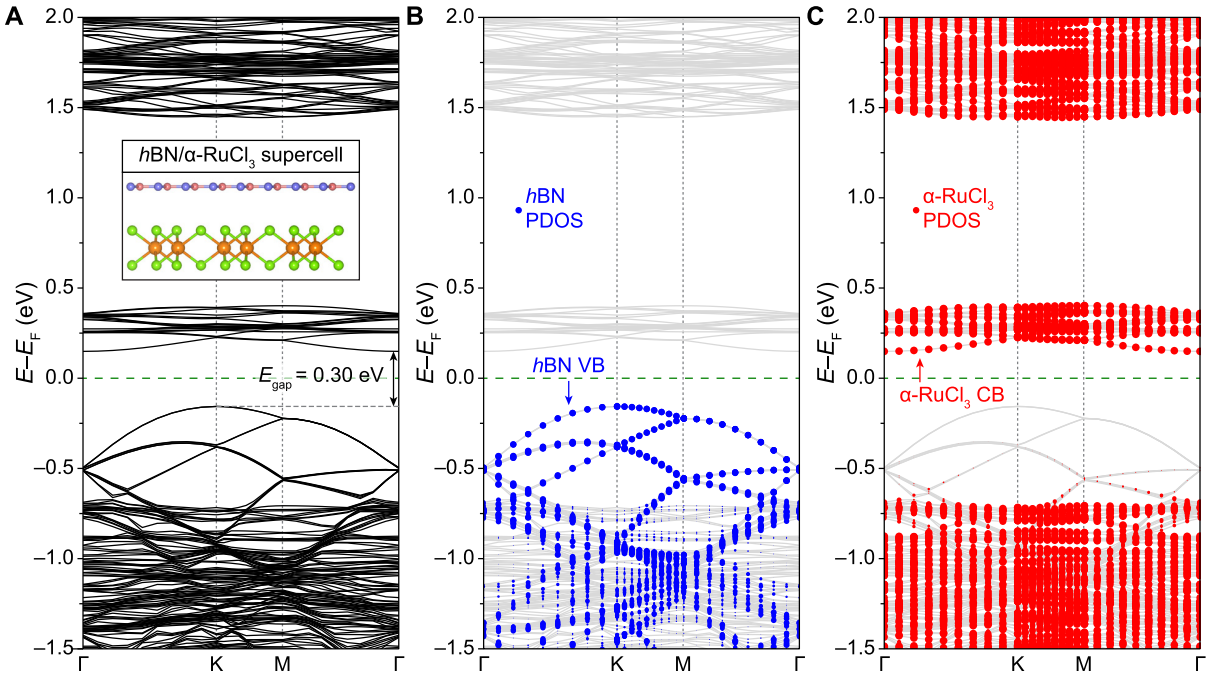

Figure 4. Theoretical electronic structure of hBN/α-$RuCl_3$ heterostructures. (A) The calculated band structure for the supercell shown in the inset (the same supercell is used for the Bader charge shown in Figure 1C). (B) The same band structure in panel A overlaid with the projected bands for hBN (solid blue circles) and (C) overlaid with the project bands for α-$RuCl_3$ (solid red circles). The area of the circles is proportional to the projected density of states at a given value of k. For all panels, the Fermi energy E_F is denoted by the horizontal dashed green lines, and the K and M points are denoted by vertical dotted gray lines.

(Figure 3A). Thus, we extracted the average S_4 and Φ_4 in both regions and plotted their relative contrast as a function of frequency to reveal a clear systematic Lorentzian-like resonance centered around 1550 cm^{-1} (solid circles in Figure 3B). Conversely, the use of intrinsic optical parameters to calculate the expected ellipsoidal tip-enhanced near-field spectrum for our experimental stack (i.e., the lightning-rod model,[76] see SI) displays no such resonance (solid black lines in Figure 3B). Therefore, as with the PhP losses, intrinsic optical parameters fail to capture the observed nano-optical behavior of hBN/α-$RuCl_3$ heterostructures.

We proceed with a phenomenological description of the novel resonance at 1550 cm^{-1} in order to reconcile our experimental observations with models of the PhP losses and near-field spectroscopy. To achieve this, we model the hBN/α-$RuCl_3$ interface by adding a single Lorentzian oscillator to the α-$RuCl_3$ side of the interface (i.e., assuming only a very thin layer of modified optical properties at the interface, consistent with calculations of similar 2D charge-transfer interfaces).[58] By fitting the oscillator parameters to the experimental spectra in Figure 3B, we find that the agreement between the lightning rod model and our experimental spectra is significantly improved (dashed black lines in Figure 3B). Moreover, incorporation of these modified optical parameters into our calculation of the PhP Q factors gives significantly improved agreement between theory and experiment (Figure 2C), while the model dispersion now slightly overestimates the experimental values (Figure S2C). This is consistent with the observation that the frequencies at which Q_S and Q_R deviate most significantly align with the onset of this novel spectroscopic resonance (Figures 3B, S4). Therefore, the totality of our nano-optical measurements reveals that the hBN/α-$RuCl_3$ interfacial dipole layer damps PhPs that possess significant out-of-plane components, giving rise to an emergent optical response that empirically takes the form of a Lorentzian oscillator.

In order to better understand the microscopic origin of excess optical losses at hBN/α-$RuCl_3$ interfaces, we performed a series of *ab initio* calculations for monolayer hBN, monolayer α-$RuCl_3$, and monolayer-on-monolayer hBN/α-$RuCl_3$ (Figures 4A, S5; see Methods section and ref 58 for details). We observe that in their free-standing states, the hBN valence band (VB) and the α-$RuCl_3$ conduction band (CB) are energetically aligned relative to the vacuum energy (Figure S5D,E), as observed previously.[77] When the hBN/α-$RuCl_3$ heterostructure is formed, the work-function-induced interfacial dipole causes these two bands to split in energy, leading to a band gap of E_g = 0.3 eV (Figures 4A, S5F). Referenced to the vacuum level, the relative decrease of the hBN VB energy compared to the α-$RuCl_3$ CB energy is consistent with electron-donor behavior in hBN and electron-acceptor behavior in α-$RuCl_3$ (Figures 1C, S5D−F). We verify this interpretation by calculating the projected bands in each layer (Figure 4B,C), which show that the combined low-energy band structure of hBN/α-$RuCl_3$ is essentially a superposition of the α-$RuCl_3$ CB and the hBN VB, with each residing substantially closer to E_F than in their intrinsic state (Figure S5A−C). Thus, the formation of an interfacial dipole is concurrent with the renormalization of the component band structures relative to the vacuum level, albeit without any associated free charge carriers. One can therefore interpret the charge transfer and associated dipole moment calculated in Figure 1C as emerging from the out-of-plane distortion of electronic orbitals in each layer and not the emptying or filling of interfacial electronic states.

It is instructive to consider that additional interfacial effects may be influencing our experimental results that are not captured in the single-particle picture presented in Figure 4.

https://doi.org/10.1021/acs.nanolett.3c01611
Nano Lett. XXXX, XXX, XXX−XXX

For instance, it is known that *h*BN can possess defect states[33−37] that may act as local reservoirs for interfacial charge transfer. Moreover, in its intrinsic state, α-$RuCl_3$ is a Mott insulator that undergoes significant correlation-induced band structure renormalization upon doping that would not be captured by single-particle DFT calculations. For instance, evidence of intragap states and the redistribution of state density between the lower and upper Hubbard bands (LHB and UHB, respectively) has been seen in recent studies of α-$RuCl_3$ with electron-doping intercalates.[78,79] Electron-doping of α-$RuCl_3$ in these intercalated structures greatly enhances the optical conductivity over a broad range of infrared frequencies that are inactive in the intrinsic α-$RuCl_3$ structure. Similar behavior has also been observed in α-$RuCl_3$ that has been electron-doped via charge transfer with graphene.[58] Therefore, we speculate that the strong enhancement of optical losses in *h*BN/α-$RuCl_3$ interfaces may also be associated with ionized defect states, intragap states, or shifts in the LHB or UHB of α-$RuCl_3$ upon doping with electrons.

OUTLOOK

The experimental and theoretical results presented in this work are significant for the future study of confined light, vdW heterostructures, and charge-transfer doping in 2D materials. The observation of emergent optoelectronic properties at the interface of two 2D insulators is reminiscent of 2D electron gases (2DEGS) formed at the interface of GaAs and AlGaAs MOSFET devices.[80] The ability to realize analogous structures in 2D heterostructures presents opportunities for using large work function materials such as α-$RuCl_3$ to gain access to deep-lying occupied states that do not normally participate in electronic transport. Such structures can, in principle, be further modified with an electrostatic gate, offering additional means of tuning normally inaccessible states. On the other hand, α-$RuCl_3$ itself is a correlated insulator that is notoriously difficult to dope with a standard electrostatic gate. Our results demonstrate that normally passive adlayers such as *h*BN can have a significant influence on the α-$RuCl_3$ band alignment and can play an active role in electrostatic doping of single layers.

These results are also important in that they provide additional design criteria for 2D materials that are not often considered during device fabrication. Ostensibly, a substantial enough work function mismatch is sufficient to significantly modify the interfacial optoelectronic properties of both *h*BN and α-$RuCl_3$, despite their intrinsic insulating and low-loss behavior. While this may be a property that can be exploited, it may also give rise to deleterious behavior (such as losses) in electronic or optical devices (e.g., cavities and waveguides) for which this behavior must be taken into account.

METHODS

Experimental and theoretical methods can be found in the Supporting Information.

ASSOCIATED CONTENT

Data Availability Statement

All data presented in the manuscript are available upon request.

Supporting Information

The Supporting Information is available free of charge at https://pubs.acs.org/doi/10.1021/acs.nanolett.3c01611.

Additional details about sample fabrication, frequency-dependent s-SNOM measurements, model r_p calculations, near-field nano-optical spectroscopy measurements, and experimental and theoretical methods (PDF)

AUTHOR INFORMATION

Corresponding Authors

D. N. Basov − *Department of Physics, Columbia University, New York, New York 10027, United States*; Email: db3056@columbia.edu

Cory R. Dean − *Department of Physics, Columbia University, New York, New York 10027, United States*; Email: cd2478@columbia.edu

Angel Rubio − *Theory Department, Max Planck Institute for Structure and Dynamics of Matter and Center for Free-Electron Laser Science, 22761 Hamburg, Germany; Center for Computational Quantum Physics, Flatiron Institute, New York, New York 10010, United States; Nano-Bio Spectroscopy Group, Universidad del País Vasco UPV/EHU, San Sebastián 20018, Spain*; orcid.org/0000-0003-2060-3151; Email: angel.rubio@mpsd.mpg.de

Daniel J. Rizzo − *Department of Physics, Columbia University, New York, New York 10027, United States*; orcid.org/0000-0003-4587-4863; Email: djr2181@columbia.edu

Authors

Jin Zhang − *Theory Department, Max Planck Institute for Structure and Dynamics of Matter and Center for Free-Electron Laser Science, 22761 Hamburg, Germany*; orcid.org/0000-0001-7830-3464

Bjarke S. Jessen − *Department of Physics, Columbia University, New York, New York 10027, United States*; orcid.org/0000-0001-8453-6125

Francesco L. Ruta − *Department of Physics and Department of Applied Physics and Applied Mathematics, Columbia University, New York, New York 10027, United States*; orcid.org/0000-0002-8746-9420

Matthew Cothrine − *Department of Materials Science and Engineering, University of Tennessee, Knoxville, Tennessee 37996, United States*

Jiaqiang Yan − *Department of Materials Science and Engineering, University of Tennessee, Knoxville, Tennessee 37996, United States; Materials Science and Technology Division, Oak Ridge National Laboratory, Oak Ridge, Tennessee 37831, United States*; orcid.org/0000-0001-6625-4706

David G. Mandrus − *Department of Materials Science and Engineering, University of Tennessee, Knoxville, Tennessee 37996, United States; Materials Science and Technology Division, Oak Ridge National Laboratory, Oak Ridge, Tennessee 37831, United States*; orcid.org/0000-0003-3616-7104

Stephen E. Nagler − *Neutron Scattering Division, Oak Ridge National Laboratory, Oak Ridge, Tennessee 37831, United States; Department of Physics and Astronomy, University of Tennessee, Knoxville, Tennessee 37996, United States*

Takashi Taniguchi − *Research Center for Materials Nanoarchitectonics, National Institute for Materials Science, Tsukuba 305-0044, Japan*; orcid.org/0000-0002-1467-3105

https://doi.org/10.1021/acs.nanolett.3c01611
Nano Lett. XXXX, XXX, XXX−XXX

Kenji Watanabe − *Research Center for Electronic and Optical Materials, National Institute for Materials Science, Tsukuba 305-0044, Japan;* orcid.org/0000-0003-3701-8119
Michael M. Fogler − *Department of Physics, University of California San Diego, La Jolla, California 92093, United States*
Abhay N. Pasupathy − *Department of Physics, Columbia University, New York, New York 10027, United States;* orcid.org/0000-0002-2744-0634
Andrew J. Millis − *Department of Physics, Columbia University, New York, New York 10027, United States; Center for Computational Quantum Physics, Flatiron Institute, New York, New York 10010, United States*
James C. Hone − *Department of Mechanical Engineering, Columbia University, New York, New York 10027, United States;* orcid.org/0000-0002-8084-3301

Complete contact information is available at: https://pubs.acs.org/10.1021/acs.nanolett.3c01611

Author Contributions

[&]D.J.R. and J.Z. contributed equally to this paper. D.J.R. performed all s-SNOM measurements and analysis. F.L.R. modeled the near-field data. J.Z. and A.R. performed all the DFT calculations and theoretical modeling and analyzed the results. B.S.J. fabricated the devices and developed the dry stacking procedure with α-$RuCl_3$. J.C.H. and C.R.D. advised device fabrication efforts. M.C., S.E.N., J.Q.Y., and D.G.M. performed growth and characterization of α-$RuCl_3$ single crystals. K.W. and T.T. performed growth and characterization of *h*BN single crystals. The manuscript was written with input from all authors.

Notes

The authors declare no competing financial interest.

ACKNOWLEDGMENTS

Research at Columbia University was supported as part of the Energy Frontier Research Center on Programmable Quantum Materials funded by the U.S. Department of Energy (DOE), Office of Science, Basic Energy Sciences (BES), under award no. DE-SC0019443. J.Z. and A.R. were supported by the Cluster of Excellence "Advanced Imaging of Matter" (AIM) EXC 2056-390715994, funding by the Deutsche Forschungsgemeinschaft (DFG, German Research Foundation) under RTG 2247, Grupos Consolidados (IT1249-19) and SFB925 "Light induced dynamics and control of correlated quantum systems". J.Z. and A.R. would like to acknowledge Nicolas Tancogne-Dejean and Lede Xian for fruitful discussions and also acknowledge support by the Max Planck Institute—New York City Center for Non-Equilibrium Quantum Phenomena. The Flatiron Institute is a division of the Simons Foundation. J.Z. acknowledges funding received from the European Union Horizon 2020 research and innovation program under Marie Sklodowska-Curie Grant Agreement 886291 (PeSD-NeSL). K.W. and T.T. acknowledge support from the JSPS KAKENHI (Grant Numbers 20H00354, 21H05233, and 23H02052) and World Premier International Research Center Initiative (WPI), MEXT, Japan. J.Q.Y. was supported by the U.S. Department of Energy, Office of Science, Basic Energy Sciences, Materials Sciences and Engineering Division. S.E.N. received support from the Quantum Science Center (QSC), a National Quantum Information Science Research Center of the U.S. Department of Energy (DOE). D.G.M. acknowledges support from the Gordon and Betty Moore Foundation's EPiQS Initiative, Grant GBMF906.

REFERENCES

(1) Huang, B.; Clark, G.; Navarro-Moratalla, E.; Klein, D. R.; Cheng, R.; Seyler, K. L.; Zhong, D.; Schmidgall, E.; McGuire, M. A.; Cobden, D. H.; Yao, W.; Xiao, D.; Jarillo-Herrero, P.; Xu, X. Layer-Dependent Ferromagnetism in a Van Der Waals Crystal Down to the Monolayer Limit. *Nature* **2017**, *546*, 270−273.
(2) Gong, C.; Li, L.; Li, Z.; Ji, H.; Stern, A.; Xia, Y.; Cao, T.; Bao, W.; Wang, C.; Wang, Y.; Qiu, Z. Q.; Cava, R. J.; Louie, S. G.; Xia, J.; Zhang, X. Discovery of Intrinsic Ferromagnetism in Two-Dimensional Van Der Waals Crystals. *Nature* **2017**, *546*, 265−269.
(3) Abramchuk, M.; Jaszewski, S.; Metz, K. R.; Osterhoudt, G. B.; Wang, Y.; Burch, K. S.; Tafti, F. Controlling Magnetic and Optical Properties of the Van Der Waals Crystal $CrCl_{3-x}Br_x$ Via Mixed Halide Chemistry. *Adv. Mater.* **2018**, *30*, 1801325.
(4) Burch, K. S.; Mandrus, D.; Park, J.-G. Magnetism in Two-Dimensional Van Der Waals Materials. *Nature* **2018**, *563*, 47−52.
(5) Jiang, S.; Shan, J.; Mak, K. F. Electric-Field Switching of Two-Dimensional Van Der Waals Magnets. *Nat. Mater.* **2018**, *17*, 406−410.
(6) Klein, D. R.; MacNeill, D.; Lado, J. L.; Soriano, D.; Navarro-Moratalla, E.; Watanabe, K.; Taniguchi, T.; Manni, S.; Canfield, P.; Fernández-Rossier, J.; Jarillo-Herrero, P. Probing Magnetism in 2D Van Der Waals Crystalline Insulators Via Electron Tunneling. *Science* **2018**, *360*, 1218−1222.
(7) Rizzo, D. J.; McLeod, A. S.; Carnahan, C.; Telford, E. J.; Dismukes, A. H.; Wiscons, R. A.; Dong, Y.; Nuckolls, C.; Dean, C. R.; Pasupathy, A. N.; Roy, X.; Xiao, D.; Basov, D. N. Visualizing Atomically Layered Magnetism in CrSBr. *Adv. Mater.* **2022**, *34*, 2201000.
(8) Telford, E. J.; Dismukes, A. H.; Dudley, R. L.; Wiscons, R. A.; Lee, K.; Chica, D. G.; Ziebel, M. E.; Han, M.-G.; Yu, J.; Shabani, S.; Scheie, A.; Watanabe, K.; Taniguchi, T.; Xiao, D.; Zhu, Y.; Pasupathy, A. N.; Nuckolls, C.; Zhu, X.; Dean, C. R.; Roy, X. Coupling between Magnetic Order and Charge Transport in a Two-Dimensional Magnetic Semiconductor. *Nat. Mater.* **2022**, *21*, 754−760.
(9) Lee, K.; Dismukes, A. H.; Telford, E. J.; Wiscons, R. A.; Wang, J.; Xu, X.; Nuckolls, C.; Dean, C. R.; Roy, X.; Zhu, X. Magnetic Order and Symmetry in the 2d Semiconductor CrSBr. *Nano Lett.* **2021**, *21*, 3511−3517.
(10) Pedramrazi, Z.; Herbig, C.; Pulkin, A.; Tang, S.; Phillips, M.; Wong, D.; Ryu, H.; Pizzochero, M.; Chen, Y.; Wang, F.; Mele, E. J.; Shen, Z.-X.; Mo, S.-K.; Yazyev, O. V.; Crommie, M. F. Manipulating Topological Domain Boundaries in the Single-Layer Quantum Spin Hall Insulator 1T′−WSe_2. *Nano Lett.* **2019**, *19*, 5634−5639.
(11) Ugeda, M. M.; Pulkin, A.; Tang, S.; Ryu, H.; Wu, Q.; Zhang, Y.; Wong, D.; Pedramrazi, Z.; Martín-Recio, A.; Chen, Y.; Wang, F.; Shen, Z.-X.; Mo, S.-K.; Yazyev, O. V.; Crommie, M. F. Observation of Topologically Protected States at Crystalline Phase Boundaries in Single-Layer WSe_2. *Nat. Commun.* **2018**, *9*, 3401.
(12) Sajadi, E.; Palomaki, T.; Fei, Z.; Zhao, W.; Bement, P.; Olsen, C.; Luescher, S.; Xu, X.; Folk, J. A.; Cobden, D. H. Gate-Induced Superconductivity in a Monolayer Topological Insulator. *Science* **2018**, *362*, 922−925.
(13) Shi, Y.; Kahn, J.; Niu, B.; Fei, Z.; Sun, B.; Cai, X.; Francisco, B. A.; Wu, D.; Shen, Z.-X.; Xu, X.; Cobden, D. H.; Cui, Y.-T. Imaging Quantum Spin Hall Edges in Monolayer WTe_2. *Sci. Adv.* **2019**, *5*, eaat8799.
(14) Kane, C. L.; Mele, E. J. Z_2 Topological Order and the Quantum Spin Hall Effect. *Phys. Rev. Lett.* **2005**, *95*, 146802.
(15) Cazalilla, M. A.; Ochoa, H.; Guinea, F. Quantum Spin Hall Effect in Two-Dimensional Crystals of Transition-Metal Dichalcogenides. *Phys. Rev. Lett.* **2014**, *113*, No. 077201.
(16) Kou, L.; Ma, Y.; Sun, Z.; Heine, T.; Chen, C. Two-Dimensional Topological Insulators: Progress and Prospects. *J. Phys. Chem. Lett.* **2017**, *8*, 1905−1919.

(17) Chen, Y.; Ruan, W.; Wu, M.; Tang, S.; Ryu, H.; Tsai, H.-Z.; Lee, R. L.; Kahn, S.; Liou, F.; Jia, C.; Albertini, O. R.; Xiong, H.; Jia, T.; Liu, Z.; Sobota, J. A.; Liu, A. Y.; Moore, J. E.; Shen, Z.-X.; Louie, S. G.; Mo, S.-K.; Crommie, M. F. Strong Correlations and Orbital Texture in Single-Layer 1T-$TaSe_2$. *Nat. Phys.* **2020**, *16*, 218−224.
(18) Cao, Y.; Fatemi, V.; Demir, A.; Fang, S.; Tomarken, S. L.; Luo, J. Y.; Sanchez-Yamagishi, J. D.; Watanabe, K.; Taniguchi, T.; Kaxiras, E.; Ashoori, R. C.; Jarillo-Herrero, P. Correlated Insulator Behaviour at Half-Filling in Magic-Angle Graphene Superlattices. *Nature* **2018**, *556*, 80−84.
(19) Chen, G.; Jiang, L.; Wu, S.; Lyu, B.; Li, H.; Chittari, B. L.; Watanabe, K.; Taniguchi, T.; Shi, Z.; Jung, J.; Zhang, Y.; Wang, F. Evidence of a Gate-Tunable Mott Insulator in a Trilayer Graphene Moiré Superlattice. *Nat. Phys.* **2019**, *15*, 237−241.
(20) Ma, L.; Ye, C.; Yu, Y.; Lu, X. F.; Niu, X.; Kim, S.; Feng, D.; Tománek, D.; Son, Y.-W.; Chen, X. H.; Zhang, Y. A Metallic Mosaic Phase and the Origin of Mott-Insulating State in 1T-TaS_2. *Nat. Commun.* **2016**, *7*, 10956.
(21) Wang, L.; Shih, E.-M.; Ghiotto, A.; Xian, L.; Rhodes, D. A.; Tan, C.; Claassen, M.; Kennes, D. M.; Bai, Y.; Kim, B.; Watanabe, K.; Taniguchi, T.; Zhu, X.; Hone, J.; Rubio, A.; Pasupathy, A. N.; Dean, C. R. Correlated Electronic Phases in Twisted Bilayer Transition Metal Dichalcogenides. *Nat. Mater.* **2020**, *19*, 861−866.
(22) Yankowitz, M.; Chen, S.; Polshyn, H.; Zhang, Y.; Watanabe, K.; Taniguchi, T.; Graf, D.; Young, A. F.; Dean, C. R. Tuning Superconductivity in Twisted Bilayer Graphene. *Science* **2019**, *363*, 1059−1064.
(23) Cao, Y.; Fatemi, V.; Fang, S.; Watanabe, K.; Taniguchi, T.; Kaxiras, E.; Jarillo-Herrero, P. Unconventional Superconductivity in Magic-Angle Graphene Superlattices. *Nature* **2018**, *556*, 43−50.
(24) Chen, G.; Sharpe, A. L.; Gallagher, P.; Rosen, I. T.; Fox, E. J.; Jiang, L.; Lyu, B.; Li, H.; Watanabe, K.; Taniguchi, T.; Jung, J.; Shi, Z.; Goldhaber-Gordon, D.; Zhang, Y.; Wang, F. Signatures of Tunable Superconductivity in a Trilayer Graphene Moiré Superlattice. *Nature* **2019**, *572*, 215−219.
(25) Onishi, S.; Ugeda, M. M.; Zhang, Y.; Chen, Y.; Ojeda-Aristizabal, C.; Ryu, H.; Mo, S.-K.; Hussain, Z.; Shen, Z.-X.; Crommie, M. F.; Zettl, A. Selenium Capped Monolayer $NbSe_2$ for Two-Dimensional Superconductivity Studies. *physica status solidi (b)* **2016**, *253*, 2396−2399.
(26) Saito, Y.; Nojima, T.; Iwasa, Y. Highly Crystalline 2D Superconductors. *Nature Reviews Materials* **2017**, *2*, 16094.
(27) Jiang, D.; Hu, T.; You, L.; Li, Q.; Li, A.; Wang, H.; Mu, G.; Chen, Z.; Zhang, H.; Yu, G.; Zhu, J.; Sun, Q.; Lin, C.; Xiao, H.; Xie, X.; Jiang, M. High-T_c Superconductivity in Ultrathin $Bi_2Sr_2CaCu_2O_{8+x}$ Down to Half-Unit-Cell Thickness by Protection with Graphene. *Nat. Commun.* **2014**, *5*, 1−6.
(28) Xi, X.; Zhao, L.; Wang, Z.; Berger, H.; Forró, L.; Shan, J.; Mak, K. F. Strongly Enhanced Charge-Density-Wave Order in Monolayer $NbSe_2$. *Nat. Nanotechnol.* **2015**, *10*, 765−769.
(29) Cassabois, G.; Valvin, P.; Gil, B. Hexagonal Boron Nitride Is an Indirect Bandgap Semiconductor. *Nat. Photonics* **2016**, *10*, 262−266.
(30) Elias, C.; Valvin, P.; Pelini, T.; Summerfield, A.; Mellor, C. J.; Cheng, T. S.; Eaves, L.; Foxon, C. T.; Beton, P. H.; Novikov, S. V.; Gil, B.; Cassabois, G. Direct Band-Gap Crossover in Epitaxial Monolayer Boron Nitride. *Nat. Commun.* **2019**, *10*, 2639.
(31) Wang, L.; Meric, I.; Huang, P. Y.; Gao, Q.; Gao, Y.; Tran, H.; Taniguchi, T.; Watanabe, K.; Campos, L. M.; Muller, D. A.; Guo, J.; Kim, P.; Hone, J.; Shepard, K. L.; Dean, C. R. One-Dimensional Electrical Contact to a Two-Dimensional Material. *Science* **2013**, *342*, 614−617.
(32) Dean, C. R.; Young, A. F.; Meric, I.; Lee, C.; Wang, L.; Sorgenfrei, S.; Watanabe, K.; Taniguchi, T.; Kim, P.; Shepard, K. L.; Hone, J. Boron Nitride Substrates for High-Quality Graphene Electronics. *Nat. Nanotechnol.* **2010**, *5*, 722−726.
(33) Lee, J.; Wong, D.; Velasco, J., Jr; Rodriguez-Nieva, J. F.; Kahn, S.; Tsai, H.-Z.; Taniguchi, T.; Watanabe, K.; Zettl, A.; Wang, F.; Levitov, L. S.; Crommie, M. F. Imaging Electrostatically Confined Dirac Fermions in Graphene Quantum Dots. *Nat. Phys.* **2016**, *12*, 1032−1036.
(34) Velasco, J.; Ju, L.; Wong, D.; Kahn, S.; Lee, J.; Tsai, H.-Z.; Germany, C.; Wickenburg, S.; Lu, J.; Taniguchi, T.; Watanabe, K.; Zettl, A.; Wang, F.; Crommie, M. F. Nanoscale Control of Rewriteable Doping Patterns in Pristine Graphene/Boron Nitride Heterostructures. *Nano Lett.* **2016**, *16*, 1620−1625.
(35) Ge, Z.; Wong, D.; Lee, J.; Joucken, F.; Quezada-Lopez, E. A.; Kahn, S.; Tsai, H.-Z.; Taniguchi, T.; Watanabe, K.; Wang, F.; Zettl, A.; Crommie, M. F.; Velasco, J. Imaging Quantum Interference in Stadium-Shaped Monolayer and Bilayer Graphene Quantum Dots. *Nano Lett.* **2021**, *21*, 8993−8998.
(36) Gutiérrez, C.; Walkup, D.; Ghahari, F.; Lewandowski, C.; Rodriguez-Nieva, J. F.; Watanabe, K.; Taniguchi, T.; Levitov, L. S.; Zhitenev, N. B.; Stroscio, J. A. Interaction-Driven Quantum Hall Wedding Cake−Like Structures in Graphene Quantum Dots. *Science* **2018**, *361*, 789−794.
(37) Behn, W. A.; Krebs, Z. J.; Smith, K. J.; Watanabe, K.; Taniguchi, T.; Brar, V. W. Measuring and Tuning the Potential Landscape of Electrostatically Defined Quantum Dots in Graphene. *Nano Lett.* **2021**, *21*, 5013−5020.
(38) Yasuda, K.; Wang, X.; Watanabe, K.; Taniguchi, T.; Jarillo-Herrero, P. Stacking-Engineered Ferroelectricity in Bilayer Boron Nitride. *Science* **2021**, *372*, 1458−1462.
(39) Moore, S. L.; Ciccarino, C. J.; Halbertal, D.; McGilly, L. J.; Finney, N. R.; Yao, K.; Shao, Y.; Ni, G.; Sternbach, A.; Telford, E. J.; Kim, B. S.; Rossi, S. E.; Watanabe, K.; Taniguchi, T.; Pasupathy, A. N.; Dean, C. R.; Hone, J.; Schuck, P. J.; Narang, P.; Basov, D. N. Nanoscale Lattice Dynamics in Hexagonal Boron Nitride Moiré Superlattices. *Nat. Commun.* **2021**, *12*, 5741.
(40) Dai, S.; Fang, W.; Rivera, N.; Stehle, Y.; Jiang, B.-Y.; Shen, J.; Tay, R. Y.; Ciccarino, C. J.; Ma, Q.; Rodan-Legrain, D.; Jarillo-Herrero, P.; Teo, E. H. T.; Fogler, M. M.; Narang, P.; Kong, J.; Basov, D. N. Phonon Polaritons in Monolayers of Hexagonal Boron Nitride. *Adv. Mater.* **2019**, *31*, 1806603.
(41) Lee, I.-H.; He, M.; Zhang, X.; Luo, Y.; Liu, S.; Edgar, J. H.; Wang, K.; Avouris, P.; Low, T.; Caldwell, J. D.; Oh, S.-H. Image Polaritons in Boron Nitride for Extreme Polariton Confinement with Low Losses. *Nat. Commun.* **2020**, *11*, 3649.
(42) Dai, S.; Fei, Z.; Ma, Q.; Rodin, A. S.; Wagner, M.; McLeod, A. S.; Liu, M. K.; Gannett, W.; Regan, W.; Watanabe, K.; Taniguchi, T.; Thiemens, M.; Dominguez, G.; Neto, A. H. C.; Zettl, A.; Keilmann, F.; Jarillo-Herrero, P.; Fogler, M. M.; Basov, D. N. Tunable Phonon Polaritons in Atomically Thin Van Der Waals Crystals of Boron Nitride. *Science* **2014**, *343*, 1125−1129.
(43) Shi, Z.; Bechtel, H. A.; Berweger, S.; Sun, Y.; Zeng, B.; Jin, C.; Chang, H.; Martin, M. C.; Raschke, M. B.; Wang, F. Amplitude- and Phase-Resolved Nanospectral Imaging of Phonon Polaritons in Hexagonal Boron Nitride. *ACS Photonics* **2015**, *2*, 790−796.
(44) Giles, A. J.; Dai, S.; Vurgaftman, I.; Hoffman, T.; Liu, S.; Lindsay, L.; Ellis, C. T.; Assefa, N.; Chatzakis, I.; Reinecke, T. L.; Tischler, J. G.; Fogler, M. M.; Edgar, J. H.; Basov, D. N.; Caldwell, J. D. Ultralow-Loss Polaritons in Isotopically Pure Boron Nitride. *Nat. Mater.* **2018**, *17*, 134−139.
(45) Brar, V. W.; Jang, M. S.; Sherrott, M.; Kim, S.; Lopez, J. J.; Kim, L. B.; Choi, M.; Atwater, H. Hybrid Surface-Phonon-Plasmon Polariton Modes in Graphene/Monolayer h-BN Heterostructures. *Nano Lett.* **2014**, *14*, 3876−3880.
(46) Jia, Y.; Zhao, H.; Guo, Q.; Wang, X.; Wang, H.; Xia, F. Tunable Plasmon−Phonon Polaritons in Layered Graphene−Hexagonal Boron Nitride Heterostructures. *ACS Photonics* **2015**, *2*, 907−912.
(47) Dai, S.; Ma, Q.; Liu, M. K.; Andersen, T.; Fei, Z.; Goldflam, M. D.; Wagner, M.; Watanabe, K.; Taniguchi, T.; Thiemens, M.; Keilmann, F.; Janssen, G. C. A. M.; Zhu, S. E.; Jarillo-Herrero, P.; Fogler, M. M.; Basov, D. N. Graphene on Hexagonal Boron Nitride as a Tunable Hyperbolic Metamaterial. *Nat. Nanotechnol.* **2015**, *10*, 682−686.
(48) Ramer, G.; Tuteja, M.; Matson, J. R.; Davanco, M.; Folland, T. G.; Kretinin, A.; Taniguchi, T.; Watanabe, K.; Novoselov, K. S.;

https://doi.org/10.1021/acs.nanolett.3c01611
Nano Lett. XXXX, XXX, XXX−XXX

Caldwell, J. D.; Centrone, A. High-Q Dark Hyperbolic Phonon-Polaritons in Hexagonal Boron Nitride Nanostructures. *Nanophotonics* **2020**, *9*, 1457−1467.
(49) Li, P.; Lewin, M.; Kretinin, A. V.; Caldwell, J. D.; Novoselov, K. S.; Taniguchi, T.; Watanabe, K.; Gaussmann, F.; Taubner, T. Hyperbolic Phonon-Polaritons in Boron Nitride for Near-Field Optical Imaging and Focusing. *Nat. Commun.* **2015**, *6*, 7507.
(50) Li, P.; Dolado, I.; Alfaro-Mozaz, F. J.; Nikitin, A. Y.; Casanova, F.; Hueso, L. E.; Vélez, S.; Hillenbrand, R. Optical Nanoimaging of Hyperbolic Surface Polaritons at the Edges of Van Der Waals Materials. *Nano Lett.* **2017**, *17*, 228−235.
(51) Dai, S.; Tymchenko, M.; Yang, Y.; Ma, Q.; Pita-Vidal, M.; Watanabe, K.; Taniguchi, T.; Jarillo-Herrero, P.; Fogler, M. M.; Alù, A.; Basov, D. N. Manipulation and Steering of Hyperbolic Surface Polaritons in Hexagonal Boron Nitride. *Adv. Mater.* **2018**, *30*, 1706358.
(52) Wang, Z.; Chiu, Y.-H.; Honz, K.; Mak, K. F.; Shan, J. Electrical Tuning of Interlayer Exciton Gases in WSe_2 Bilayers. *Nano Lett.* **2018**, *18*, 137−143.
(53) Ma, L.; Nguyen, P. X.; Wang, Z.; Zeng, Y.; Watanabe, K.; Taniguchi, T.; MacDonald, A. H.; Mak, K. F.; Shan, J. Strongly Correlated Excitonic Insulator in Atomic Double Layers. *Nature* **2021**, *598*, 585−589.
(54) Tran, K.; Moody, G.; Wu, F.; Lu, X.; Choi, J.; Kim, K.; Rai, A.; Sanchez, D. A.; Quan, J.; Singh, A.; Embley, J.; Zepeda, A.; Campbell, M.; Autry, T.; Taniguchi, T.; Watanabe, K.; Lu, N.; Banerjee, S. K.; Silverman, K. L.; Kim, S.; Tutuc, E.; Yang, L.; MacDonald, A. H.; Li, X. Evidence for Moiré Excitons in Van Der Waals Heterostructures. *Nature* **2019**, *567*, 71−75.
(55) Jin, C.; Regan, E. C.; Yan, A.; Iqbal Bakti Utama, M.; Wang, D.; Zhao, S.; Qin, Y.; Yang, S.; Zheng, Z.; Shi, S.; Watanabe, K.; Taniguchi, T.; Tongay, S.; Zettl, A.; Wang, F. Observation of Moiré Excitons in WSe_2/WS_2 Heterostructure Superlattices. *Nature* **2019**, *567*, 76−80.
(56) Song, T.; Fei, Z.; Yankowitz, M.; Lin, Z.; Jiang, Q.; Hwangbo, K.; Zhang, Q.; Sun, B.; Taniguchi, T.; Watanabe, K.; McGuire, M. A.; Graf, D.; Cao, T.; Chu, J.-H.; Cobden, D. H.; Dean, C. R.; Xiao, D.; Xu, X. Switching 2D Magnetic States Via Pressure Tuning of Layer Stacking. *Nat. Mater.* **2019**, *18*, 1298−1302.
(57) Zhou, B.; Balgley, J.; Lampen-Kelley, P.; Yan, J. Q.; Mandrus, D. G.; Henriksen, E. A. Evidence for Charge Transfer and Proximate Magnetism in Graphene−α-$RuCl_3$ Heterostructures. *Phys. Rev. B* **2019**, *100*, 165426.
(58) Rizzo, D. J.; Jessen, B. S.; Sun, Z.; Ruta, F. L.; Zhang, J.; Yan, J.-Q.; Xian, L.; McLeod, A. S.; Berkowitz, M. E.; Watanabe, K.; Taniguchi, T.; Nagler, S. E.; Mandrus, D. G.; Rubio, A.; Fogler, M. M.; Millis, A. J.; Hone, J. C.; Dean, C. R.; Basov, D. N. Charge-Transfer Plasmon Polaritons at Graphene/α-$RuCl_3$ Interfaces. *Nano Lett.* **2020**, *20*, 8438−8445.
(59) Rizzo, D. J.; Shabani, S.; Jessen, B. S.; Zhang, J.; McLeod, A. S.; Rubio-Verdú, C.; Ruta, F. L.; Cothrine, M.; Yan, J.; Mandrus, D. G.; Nagler, S. E.; Rubio, A.; Hone, J. C.; Dean, C. R.; Pasupathy, A. N.; Basov, D. N. Nanometer-Scale Lateral p−n Junctions in Graphene/ Heterostructures. *Nano Lett.* **2022**, *22*, 1946−1953.
(60) Wang, Y.; Balgley, J.; Gerber, E.; Gray, M.; Kumar, N.; Lu, X.; Yan, J.-Q.; Fereidouni, A.; Basnet, R.; Yun, S. J.; Suri, D.; Kitadai, H.; Taniguchi, T.; Watanabe, K.; Ling, X.; Moodera, J.; Lee, Y. H.; Churchill, H. O. H.; Hu, J.; Yang, L.; Kim, E.-A.; Mandrus, D. G.; Henriksen, E. A.; Burch, K. S. Modulation Doping Via a Two-Dimensional Atomic Crystalline Acceptor. *Nano Lett.* **2020**, *20*, 8446−8452.
(61) Balgley, J.; Butler, J.; Biswas, S.; Ge, Z.; Lagasse, S.; Taniguchi, T.; Watanabe, K.; Cothrine, M.; Mandrus, D. G.; Velasco, J.; Valentí, R.; Henriksen, E. A. Ultrasharp Lateral p−n Junctions in Modulation-Doped Graphene. *Nano Lett.* **2022**, *22*, 4124−4130.
(62) Gerber, E.; Yao, Y.; Arias, T. A.; Kim, E.-A. Ab Initio Mismatched Interface Theory of Graphene on α-$RuCl_3$: Doping and Magnetism. *Phys. Rev. Lett.* **2020**, *124*, 106804.
(63) Mashhadi, S.; Kim, Y.; Kim, J.; Weber, D.; Taniguchi, T.; Watanabe, K.; Park, N.; Lotsch, B.; Smet, J. H.; Burghard, M.; Kern, K. Spin-Split Band Hybridization in Graphene Proximitized with α-$RuCl_3$ Nanosheets. *Nano Lett.* **2019**, *19*, 4659−4665.
(64) Biswas, S.; Li, Y.; Winter, S. M.; Knolle, J.; Valentí, R. Electronic Properties of α-$RuCl_3$ in Proximity to Graphene. *Phys. Rev. Lett.* **2019**, *123*, 237201.
(65) Ruta, F. L.; Kim, B. S. Y.; Sun, Z.; Rizzo, D. J.; McLeod, A. S.; Rajendran, A.; Liu, S.; Millis, A. J.; Hone, J. C.; Basov, D. N. Surface Plasmons Induce Topological Transition in Graphene/α-MoO_3 Heterostructures. *Nat. Commun.* **2022**, *13*, 3719.
(66) Choi, M. S.; Nipane, A.; Kim, B. S. Y.; Ziffer, M. E.; Datta, I.; Borah, A.; Jung, Y.; Kim, B.; Rhodes, D.; Jindal, A.; Lamport, Z. A.; Lee, M.; Zangiabadi, A.; Nair, M. N.; Taniguchi, T.; Watanabe, K.; Kymissis, I.; Pasupathy, A. N.; Lipson, M.; Zhu, X.; Yoo, W. J.; Hone, J.; Teherani, J. T. High Carrier Mobility in Graphene Doped Using a Monolayer of Tungsten Oxyselenide. *Nat. Electron.* **2021**, *4*, 731−739.
(67) Kim, B. S. Y.; Sternbach, A. J.; Choi, M. S.; Sun, Z.; Ruta, F. L.; Shao, Y.; McLeod, A. S.; Xiong, L.; Dong, Y.; Chung, T. S.; Rajendran, A.; Liu, S.; Nipane, A.; Chae, S. H.; Zangiabadi, A.; Xu, X.; Millis, A. J.; Schuck, P. J.; Dean, C. R.; Hone, J. C.; Basov, D. N. Ambipolar Charge-Transfer Graphene Plasmonic Cavities. *Nat. Mater.* **2023**, *22*, 838−843.
(68) Sternbach, A. J.; Vitalone, R. A.; Shabani, S.; Zhang, J.; Darlington, T. P.; Moore, S. L.; Chae, S. H.; Seewald, E.; Xu, X.; Dean, C. R.; Zhu, X.; Rubio, A.; Hone, J.; Pasupathy, A. N.; Schuck, P. J.; Basov, D. N. Quenched Excitons in WSe_2/α-$RuCl_3$ Heterostructures Revealed by Multimessenger Nanoscopy. *Nano Lett.* **2023**, *23* (11), 5070−5075.
(69) Pollini, I. Electronic Properties of the Narrow-Band Material. *Phys. Rev. B* **1996**, *53*, 12769−12776.
(70) Strand, J.; Larcher, L.; Shluger, A. L. Properties of Intrinsic Point Defects and Dimers in Hexagonal Boron Nitride. *J. Phys.: Condens. Matter* **2020**, *32*, No. 055706.
(71) Woessner, A.; Lundeberg, M. B.; Gao, Y.; Principi, A.; Alonso-González, P.; Carrega, M.; Watanabe, K.; Taniguchi, T.; Vignale, G.; Polini, M.; Hone, J.; Hillenbrand, R.; Koppens, F. H. L. Highly Confined Low-Loss Plasmons in Graphene−Boron Nitride Heterostructures. *Nat. Mater.* **2015**, *14*, 421−425.
(72) Reschke, S.; Mayr, F.; Widmann, S.; von Nidda, H.-A. K.; Tsurkan, V.; Eremin, M. V.; Do, S.-H.; Choi, K.-Y.; Wang, Z.; Loidl, A. Sub-Gap Optical Response in the Kitaev Spin-Liquid Candidate. *J. Phys.: Condens. Matter* **2018**, *30*, 475604.
(73) Kučírková, A.; Navrátil, K. Interpretation of Infrared Transmittance Spectra of SiO_2 Thin Films. *Appl. Spectrosc.* **1994**, *48*, 113−120.
(74) Caldwell, J. D.; Kretinin, A. V.; Chen, Y.; Giannini, V.; Fogler, M. M.; Francescato, Y.; Ellis, C. T.; Tischler, J. G.; Woods, C. R.; Giles, A. J.; Hong, M.; Watanabe, K.; Taniguchi, T.; Maier, S. A.; Novoselov, K. S. Sub-Diffractional Volume-Confined Polaritons in the Natural Hyperbolic Material Hexagonal Boron Nitride. *Nat. Commun.* **2014**, *5*, 5221.
(75) Dai, S.; Ma, Q.; Andersen, T.; McLeod, A. S.; Fei, Z.; Liu, M. K.; Wagner, M.; Watanabe, K.; Taniguchi, T.; Thiemens, M.; Keilmann, F.; Jarillo-Herrero, P.; Fogler, M. M.; Basov, D. N. Subdiffractional Focusing and Guiding of Polaritonic Rays in a Natural Hyperbolic Material. *Nat. Commun.* **2015**, *6*, 6963.
(76) McLeod, A. S.; Kelly, P.; Goldflam, M. D.; Gainsforth, Z.; Westphal, A. J.; Dominguez, G.; Thiemens, M. H.; Fogler, M. M.; Basov, D. N. Model for Quantitative Tip-Enhanced Spectroscopy and the Extraction of Nanoscale-Resolved Optical Constants. *Phys. Rev. B* **2014**, *90*, No. 085136.
(77) Wang, Y.; Balgley, J.; Gerber, E.; Gray, M.; Kumar, N.; Lu, X.; Yan, J.-Q.; Fereidouni, A.; Basnet, R.; Yun, S. J.; Suri, D.; Kitadai, H.; Taniguchi, T.; Watanabe, K.; Ling, X.; Moodera, J.; Lee, Y. H.; Churchill, H. O. H.; Hu, J.; Yang, L.; Kim, E.-A.; Mandrus, D. G.; Henriksen, E. A.; Burch, K. S. Modulation Doping Via a Two-Dimensional Atomic Crystalline Acceptor. *Nano Lett.* **2020**, *20*, 8446−8452.

https://doi.org/10.1021/acs.nanolett.3c01611
Nano Lett. XXXX, XXX, XXX−XXX

(78) Jo, M.-k.; Heo, H.; Lee, J.-H.; Choi, S.; Kim, A.; Jeong, H. B.; Jeong, H. Y.; Yuk, J. M.; Eom, D.; Jahng, J.; Lee, E. S.; Jung, I.-y.; Cho, S. R.; Kim, J.; Cho, S.; Kang, K.; Song, S. Enhancement of Photoresponse on Narrow-Bandgap Mott Insulator Via Intercalation. *ACS Nano* **2021**, *15*, 18113−18124.
(79) Lam, D.; Lebedev, D.; Kuo, L.; Sangwan, V. K.; Szydłowska, B. M.; Ferraresi, F.; Söll, A.; Sofer, Z.; Hersam, M. C. Liquid-Phase Exfoliation of Magnetically and Optoelectronically Active Ruthenium Trichloride Nanosheets. *ACS Nano* **2022**, *16*, 11315−11324.
(80) Sasa, S.; Saito, J.; Nanbu, K.; Ishikawa, T.; Hiyamizu, S. Improved 2DEG Mobility in Inverted GaAs/n-AlGaAs Heterostructures Grown by MBE. *Jpn. J. Appl. Phys.* **1984**, *23*, L573.

https://doi.org/10.1021/acs.nanolett.3c01611
Nano Lett. XXXX, XXX, XXX−XXX

Supporting Information

Polaritonic probe of an emergent 2D dipole interface

Daniel J. Rizzo[1,†,*], Jin Zhang[2,†], Bjarke S. Jessen[1], Francesco L. Ruta[1,3], Matthew Cothrine[4], Jiaqiang Yan[4,5], David G. Mandrus[4,5], Stephen E. Nagler[6,7], Takashi Taniguchi[8], Kenji Watanabe[9], Michael M. Fogler[10], Abhay N. Pasupathy[1], Andrew J. Millis,[1,11] Angel Rubio[2,11,12,*], James C. Hone[13], Cory R. Dean[1,*], D.N. Basov[1,*]

[1]Department of Physics, Columbia University, New York, NY, 10027, USA

[2]Theory Department, Max Planck Institute for Structure and Dynamics of Matter and Center for Free-Electron Laser Science, 22761 Hamburg, Germany

[3]Department of Applied Physics and Applied Mathematics, Columbia University, New York, NY, 10027, USA

[4]Department of Materials Science and Engineering, University of Tennessee, Knoxville, Tennessee 37996, USA

[5]Materials Science and Technology Division, Oak Ridge National Laboratory, Oak Ridge, Tennessee 37831, USA

[6]Neutron Scattering Division, Oak Ridge 431 National Laboratory, Oak Ridge, Tennessee 37831, USA

[7]Department of Physics and Astronomy, University of Tennessee, Knoxville, Tennessee 37996, USA

[8]Research Center for Materials Nanoarchitectonics, National Institute for Materials Science, 1-1 Namiki, Tsukuba 305-0044, Japan

[9]Research Center for Electronic and Optical Materials, National Institute for Materials Science, 1-1 Namiki, Tsukuba 305-0044, Japan

[10]Department of Physics, University of California San Diego, La Jolla, California 92093, United States

[11]Center for Computational Quantum Physics, Flatiron Institute, New York, New York 10010, USA

[12]Nano-Bio Spectroscopy Group, Universidad del País Vasco UPV/EHU, San Sebastián 20018, Spain

[13]Department of Mechanical Engineering, Columbia University, New York, NY, 10027, USA

[†]D.J.R. and J.Z. contributed equally to this paper

*Correspondence to: db3056@columbia.edu, cd2478@columbia.edu, angel.rubio@mpsd.mpg.de, and djr2181@columbia.edu

Table of Contents:

Figure S1. *h*BN/α-$RuCl_3$ device fabrication	S3
Figure S2. Frequency-dependent line profiles of PhP fringes.	S4
Figure S3. Model *h*BN PhP dispersion and *Q* for different thickness of α-$RuCl_3$	S5
Figure S4. Near-field spectroscopy of *h*BN/α-$RuCl_3$ heterostructures.	S6
Figure S5. Comparison of band structures for free-standing and heterostructured *h*BN and α-$RuCl_3$.	S7
Supplementary Methods	S8
Supplementary Discussion	S10
References	S11

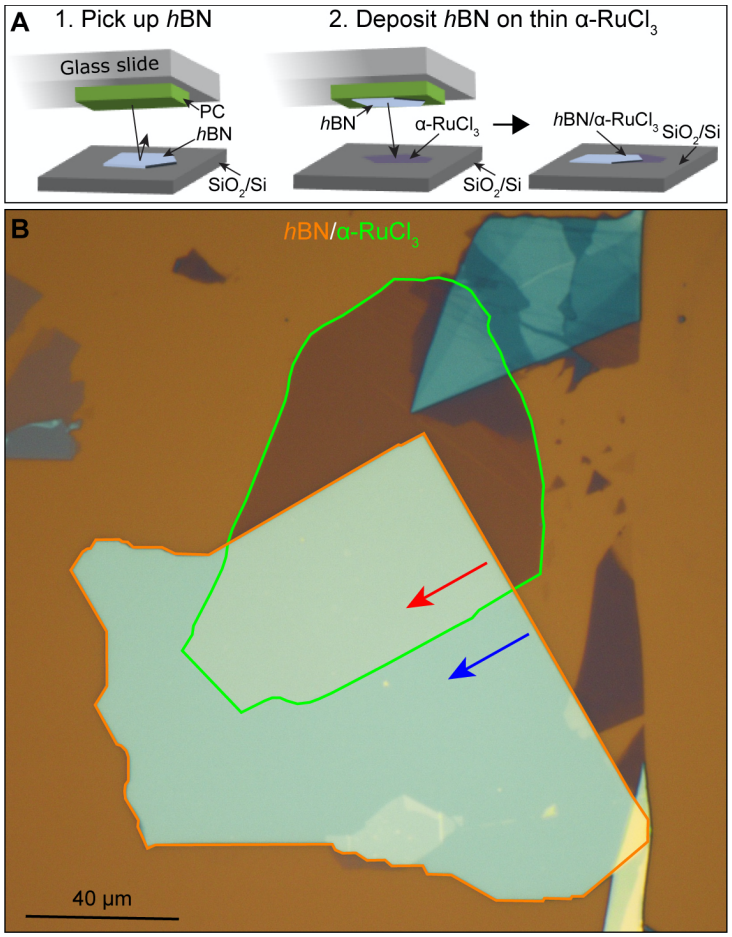

Figure S1. *h*BN/α-$RuCl_3$ device fabrication. (**A**) Diagram of two steps for *h*BN/α-$RuCl_3$ device assembly. In the first step, a PC-coated glass slide is used to pick up an exfoliated crystal of 22-nm-thick thick *h*BN on an SiO_2/Si substrate. In the second step, the *h*BN is deposited onto an exfoliated flake of few-layer α-$RuCl_3$. The final structure was constructed such that part of the *h*BN is directly on SiO_2 and part is on top of the α-$RuCl_3$. (**B**) Optical image of *h*BN/α-$RuCl_3$ device with the *h*BN outlined in orange and the α-$RuCl_3$ outlined in green. The red and blue arrows indicate the position of nano-optical imaging of PhPs on and off the α-$RuCl_3$, respectively.

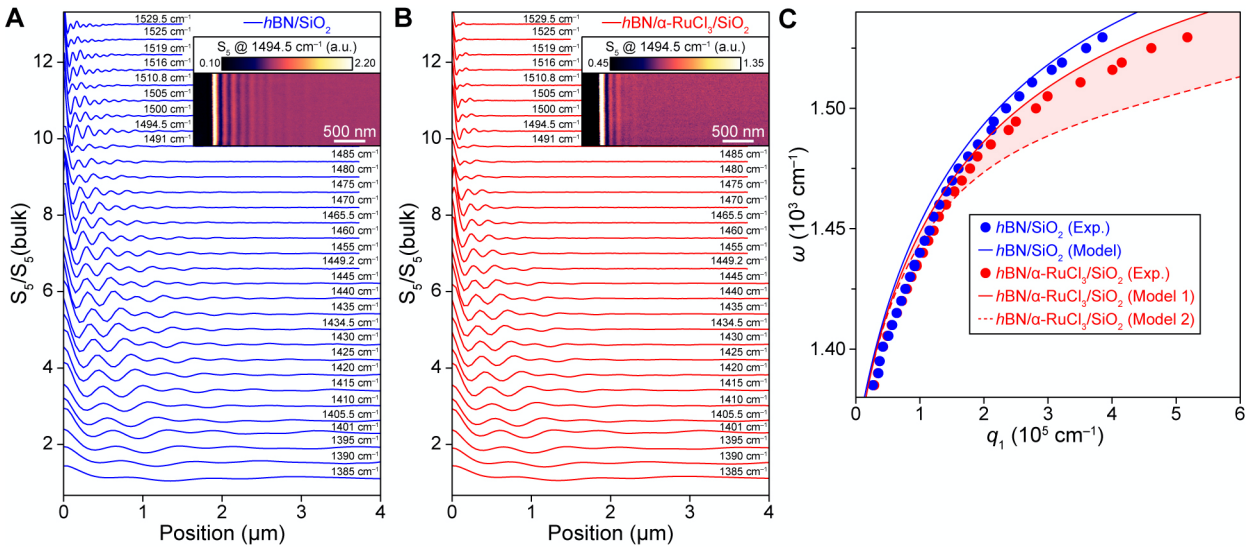

Figure S2. Frequency-dependent line profiles of PhP fringes. (**A**) Area-averaged line profiles of the near-field amplitude for *h*BN/SiO_2 showing PhP fringes collected at the indicated frequencies. A 0.4 offset is added between consecutive curves for clarity. The PhP wavelength clearly disperses with frequency. (**B**) The same as (A) but for PhPs propagating in *h*BN/α-$RuCl_3$/SiO_2. Each curve in (A) and (B) was truncated at the first minimum next to the *h*BN edge, and fit to the ansatz from refs. 1,2 to extract the complex wavevector $\boldsymbol{q}$. The ansatz is $S_0 + A\frac{e^{-iqx}}{R^a+x^a} + BH_0^{(1)}(2\boldsymbol{q}x)$, where S_0 is the bulk near-field amplitude, R is the approximate tip radius (25 nm), $H_0^{(1)}$ is the first Hankel function of order zero, A and B are sample angle- and tip-dependent scaling factors, respectively, and a is a geometric factor ≈0.1. (**C**) The experimentally extracted PhP dispersion for *h*BN on bare SiO_2 (solid blue circles) and on a layer of α-$RuCl_3$ (solid red circles). The expected PhP dispersions (i.e., maxima in $Im[r_p]$) for both regions are plotted with solid blue and solid red lines, respectively. The dashed red line shows the expected PhP dispersion when α-$RuCl_3$ is modelled with emergent interfacial losses (Model 2 in Fig. 3 of the main text), with the shaded red region highlighting the change in the dispersion.

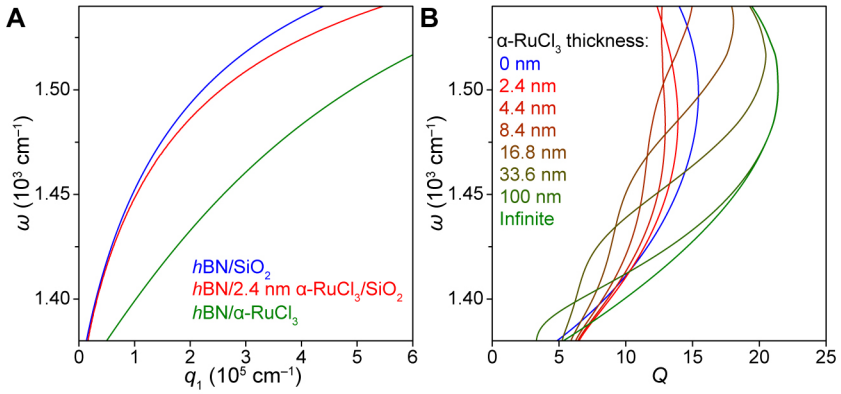

Figure S3. Model *h*BN PhP dispersion and *Q* for different thickness of α-$RuCl_3$. (**A**) The model dispersion for PhPs propagating in a 22-nm-thick *h*BN crystal on a thick slab of SiO_2 (blue curve), on a 2.4-nm-thick flake of α-$RuCl_3$ on a thick slab of SiO_2 (red curve), and on a thick slab of α-$RuCl_3$ (green curve). The dispersion is derived from maxima in the imaginary component of the *p*-polarized reflection coefficient, $Im[r_p]$. The *h*BN PhPs become more confined with thicker layers of underlying α-$RuCl_3$. (**B**) The frequency-dependent *Q* factor for PhPs propagating in a 22-nm-thick *h*BN crystal on a thick slab of SiO_2 (blue curve), on a 2.4-nm-thick flake of α-$RuCl_3$ on a thick slab of SiO_2 (red curve), and on a thick slab of α-$RuCl_3$ (green curve). The frequency-dependent *Q* is plotted for several intermediate thicknesses of α-$RuCl_3$ as indicated by the colored labels. While stacks with thinner α-$RuCl_3$ show a marginally lower value of *Q* compared to those directly on SiO_2, those with thicker α-$RuCl_3$ eventually show larger values of *Q*. The *Q* factor is calculated as outlined in the methods and supplementary discussion.

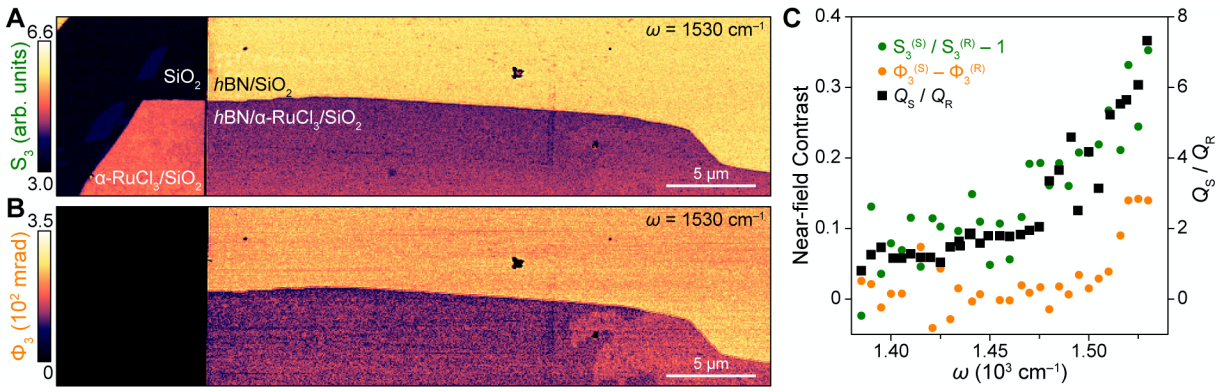

Figure S4. Near-field spectroscopy of *h*BN/α-RuCl$_3$ heterostructures. (**A**) Near-field S_3 amplitude at $\omega = 1530$ cm^{-1} of a heterostructure with *h*BN/α-RuCl$_3$/SiO$_2$, *h*BN/SiO$_2$, α-RuCl$_3$/SiO$_2$, and SiO$_2$ regions labelled. (**B**) The corresponding Φ_3 phase simultaneously collected in the same region as (A). (**C**) Plot of the frequency-dependence of the near-field contrast (solid green and orange circles are $S_3^{(S)} / S_3^{(R)} - 1$and $\Phi_3^{(S)} - \Phi_3^{(R)}$, respectively) and the ratio Q_S / Q_R (solid black squares). Here, $S_3^{(S)}$ and $S_3^{(R)}$ are the S_3 amplitudes averaged on *h*BN/SiO$_2$ and *h*BN/α-RuCl$_3$/SiO$_2$, respectively, and $\Phi_3^{(S)}$ and $\Phi_3^{(R)}$ are the Φ_3 phases averaged on *h*BN/SiO$_2$ and *h*BN/α-RuCl$_3$/SiO$_2$, respectively. The ratio between PhP *Q*-factors off and on α-RuCl$_3$ (Q_S / Q_R) increases with frequency in a manner that scales similarly to the near-field contrast.

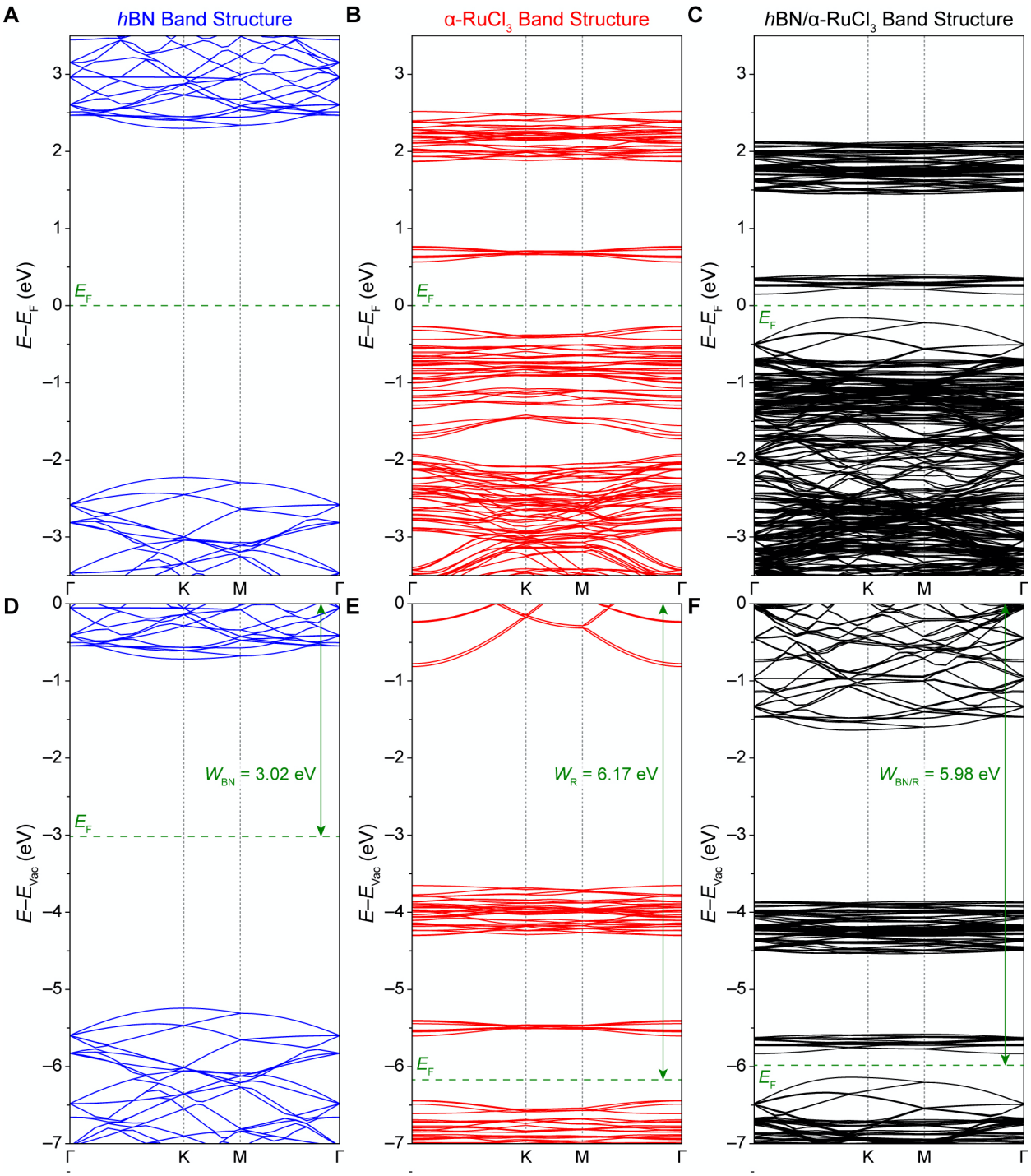

Figure S5. Comparison of band structures for free-standing and heterostructured *h*BN and α-$RuCl_3$. (**A**) Fermi energy-aligned free-standing band structures for monolayer *h*BN, (**B**) monolayer α-$RuCl_3$, and (**C**) monolayer-on-monolayer *h*BN/α-$RuCl_3$. (**D**-**E**) The same band structures plotted in (**A**-**C**) aligned relative to the vacuum energy. In their free-standing states, the *h*BN valence band (VB) is aligned energetically with the α-$RuCl_3$ conduction band (CB). The work function difference leads to the formation of an interfacial dipole in *h*BN/α-$RuCl_3$ that induces a small energy gap between the *h*BN VB and the α-$RuCl_3$ CB when heterostructured.

Supplementary Methods

Material Growth

α-$RuCl_3$ crystals were grown by the sublimation of $RuCl_3$ powder sealed in a quartz tube under vacuum. About 1 g of powder was loaded in a quartz tube of 19 mm in outer diameter, 1.5 mm thick, and 10 cm long. The growth was performed in a box furnace. After dwelling at 1060 °C for 6 h, the furnace was cooled to 800 °C at a rate of 4 °C/h. Magnetic and specific heat measurements confirmed that the as-grown pristine crystal orders antiferromagnetically around 7 K. For more information, see ref. 3.

Device Fabrication

The *h*BN/α-$RuCl_3$ heterostructures were assembled using standard dry-stacking with the hot pick-up method.[4,5] Specifically, we use a polycarbonate (PC) film on a polydimethylsiloxane (PDMS) stamp to pick up *h*BN exfoliated on a SiO_2/Si substrate at a temperature of 90 ºC. The *h*BN is then brought in contact with the target α-$RuCl_3$ crystal, also on SiO_2/Si, at a temperature of ~150 ºC. By using a higher temperature and a slow contact approach (~1 μm/min), we are able to push out most interfacial contamination, leaving us with a clean *h*BN/α-$RuCl_3$ interface. Finally, the PC film is dissolved in chloroform.

Scanning Near-field Optical Microscopy:

The s-SNOM measurements in this study were conducted using a commercial Neaspec system under ambient conditions using commercial Arrow^{TM} AFM probes with a nominal resonant frequency of f = 75 kHz. Tunable continuous wave quantum cascade lasers produced by Daylight Solutions were used spanning wavelengths from 6 to 8 μm. The detected signal was demodulated at the fourth or fifth harmonic of the tip tapping frequency in order to reduce background far-field contributions to the scattered light. The n^{th} harmonic of the near-field scattering amplitude (S_n) and phase (Φ_n) were collected simultaneously using a pseudoheterodyne interferometry technique.

Ab-initio Calculations of *h*BN/α-$RuCl_3$ Heterostructures:

The ab initio calculations were performed within the Vienna Ab initio Simulation Package (VASP)[6] using a projector-augmented wave (PAW) pseudopotential in conjunction with the Perdew–Burke–Ernzerhof (PBE)[7] functionals and plane-wave basis set with energy cutoff at 400 eV. For the heterostructures formed by *h*BN on top of a monolayer of α-$RuCl_3$, we used a fixed hexagonal supercell containing 170 atoms (composed of 3 x 3 α-$RuCl_3$ and 7 x 7 *h*BN). The resulting strain imposed on the heterostructure is ~2.1%. This strain doesn't modify the formation of the large interfacial dipole discussed in the present work. The surface Brillouin zone was sampled by a 3 × 3 × 1 Monkhorst–Pack k-mesh. A vacuum region of 15 Å was applied to avoid artificial interaction between the periodic images along the z direction. Due to the absence of strong chemical bonding between layers, we incorporate van der Waals interactions for structural optimization via the opt88 density functional introduced in ref. 8. All heterostructures for the above supercell size were fully relaxed until the force on each atom was less than 0.01 eV $Å^{-1}$. Spin-orbital couplings are included in the electronic calculations.
As shown in previous work (ref. 1) standard DFT functionals do not cope with the electronic structure of α-$RuCl_3$ as it requires accounting for on-site correlations via a Hubbard U for Ru and Cl atoms. The Hubbard U terms are computed by employing the generalized Kohn–Sham

equations within density functional theory including mean-field interactions, as provided by the Octopus package,[9,10] using the ACBN0[11,12] functional together with the local density approximation (LDA) functional describing the DFT part. We compute ab initio the Hubbard U and Hund's J for the 4d orbitals of Ruthenium and 3p orbital of Chlorine. We employ norm-conserving HGH pseudopotentials to get converged effective Hubbard U values of 1.96 eV for Ru 4d orbitals and 5.31 eV for Cl 3p orbitals, with spin-orbital couplings.

Supplementary Discussion

Calculating polariton dispersions and quality factors

Polariton dispersions $q_1(\omega)$ and quality factors $Q(\omega)$ in the main text are computed from the poles of the p-polarized reflection coefficient r_p. A condition for poles of r_p in a single finite *h*BN slab geometry corresponding to the fundamental polariton mode dispersion can be written in the following form:

$$2k_z d + \delta_{sub} + \delta_{sup} = 0$$

where $e^{i\delta_j} \approx \frac{1-i\frac{\varepsilon_j}{\sqrt{-\varepsilon_\parallel \varepsilon_z}}}{1+i\frac{\varepsilon_j}{\sqrt{-\varepsilon_\parallel \varepsilon_z}}}$ and $k_z \approx \sqrt{-\frac{\varepsilon_\parallel}{\varepsilon_\perp} q^2}$ in the near-field limit.[13] $\varepsilon_\parallel$ and $\varepsilon_\perp$ are the in- and out-of-plane dielectric functions of *h*BN, respectively,[14] and $q(\omega) = q_1(\omega) + iq_2(\omega)$ is the in-plane momentum of light. $\varepsilon_{\text{sup}} = 1$ and ε_{sub} is the dielectric function of the substrate.

For two slabs (e.g., *h*BN/α-$RuCl_3$/SiO_2 model), we solve an equivalent problem numerically. We first compute the 2x2 transfer matrix M for the system and note that $r_p = M_{21}/M_{11}$. The formalism in Reference 15 was used to compute the transfer matrix. *Nota bene*: in the case of uniaxial media like *h*BN, one should use $\varepsilon_\parallel$ (not ε_z) in Equation 10 of Reference 15. One should also ensure that the proper branches of k_z in all slabs are used such that Im $k_z \geq 0$.[16] The complex in-plane propagation constant $q(\omega)$ is obtained from minimizing $|M_{11}|$ using scipy.optimize methods. We verified that the real part $q_1(\omega)$ corresponds to the maxima of Im $r_p(q, \omega)$ and the residual $|M_{11}|^2 \sim 10^{-7}$ for all ω. Finally, we compute $Q(\omega) \equiv \frac{q_1(\omega)}{q_2(\omega)}$.
Dielectric functions of SiO_2 and α-$RuCl_3$ (assuming isotropic) are obtained from References 17 and 18, respectively.

Nano-infrared point spectra of *h*BN/SiO_2 normalized to *h*BN/α-$RuCl_3$/SiO_2 were fit by optimizing the parameters of a Lorentzian oscillator dielectric function for α-$RuCl_3$ within the lightning rod model[19] framework:

$$\varepsilon = \varepsilon_\infty + \frac{f^2}{\omega_0^2 - \omega^2 - i\gamma\omega}$$

The best-fit oscillator strength, resonance frequency, scattering rate, and background permittivity were $f = 1992\ \text{cm}^{-1}$, $\omega_0 = 1543\ \text{cm}^{-1}$, $\gamma = 30.5\ \text{cm}^{-1}$, and $\varepsilon_\infty = 2.01$, respectively. These parameters were used to compute another set of complex $q(\omega)$ that we compared with the dispersions and quality factors obtained when using the bare α-$RuCl_3$ dielectric function extracted from far-field spectroscopy in Reference 18. We note that these oscillator parameters differ significantly from those associated with nearby phonons in *h*BN or electronic transitions in α-$RuCl_3$, suggesting that this phenomenological Lorentzian oscillator cannot be trivially reproduced through rigid shifts and/or broadening of the intrinsic optical spectrum of either heterostructure constituent.

References

[1] Rizzo, D. J., Jessen, B. S., Sun, Z., Ruta, F. L., Zhang, J., Yan, J.-Q., Xian, L., McLeod, A. S., Berkowitz, M. E., Watanabe, K., Taniguchi, T., Nagler, S. E., Mandrus, D. G., Rubio, A., Fogler, M. M., Millis, A. J., Hone, J. C., Dean, C. R. & Basov, D. N. Charge-Transfer Plasmon Polaritons at Graphene/α-$RuCl_3$ Interfaces. *Nano Lett.* **20**, 8438-8445, (2020).

[2] Woessner, A., Lundeberg, M. B., Gao, Y., Principi, A., Alonso-González, P., Carrega, M., Watanabe, K., Taniguchi, T., Vignale, G., Polini, M., Hone, J., Hillenbrand, R. & Koppens, F. H. L. Highly Confined Low-Loss Plasmons in Graphene–Boron Nitride Heterostructures. *Nat. Mater.* **14**, 421-425, (2015).

[3] May, A. F., Yan, J. & McGuire, M. A. A Practical Guide for Crystal Growth of Van Der Waals Layered Materials. *J. Appl. Phys.* **128**, 051101, (2020).

[4] Pizzocchero, F., Gammelgaard, L., Jessen, B. S., Caridad, J. M., Wang, L., Hone, J., Bøggild, P. & Booth, T. J. The Hot Pick-up Technique for Batch Assembly of Van Der Waals Heterostructures. *Nat. Commun.* **7**, 11894, (2016).

[5] Purdie, D. G., Pugno, N. M., Taniguchi, T., Watanabe, K., Ferrari, A. C. & Lombardo, A. Cleaning Interfaces in Layered Materials Heterostructures. *Nat. Commun.* **9**, 5387, (2018).

[6] Kresse, G. & Furthmüller, J. Efficient Iterative Schemes for Ab Initio Total-Energy Calculations Using a Plane-Wave Basis Set. *Phys. Rev. B* **54**, 11169-11186, (1996).

[7] Perdew, J. P., Burke, K. & Ernzerhof, M. Generalized Gradient Approximation Made Simple. *Phys. Rev. Lett.* **77**, 3865-3868, (1996).

[8] Klimeš, J., Bowler, D. R. & Michaelides, A. Van Der Waals Density Functionals Applied to Solids. *Phys. Rev. B* **83**, 195131, (2011).

[9] Andrade, X., Strubbe, D., De Giovannini, U., Larsen, A. H., Oliveira, M. J. T., Alberdi-Rodriguez, J., Varas, A., Theophilou, I., Helbig, N., Verstraete, M. J., Stella, L., Nogueira, F., Aspuru-Guzik, A., Castro, A., Marques, M. A. L. & Rubio, A. Real-Space Grids and the Octopus Code as Tools for the Development of New Simulation Approaches for Electronic Systems. *Physical Chemistry Chemical Physics* **17**, 31371-31396, (2015).

[10] Tancogne-Dejean, N., Oliveira, M. J. T., Andrade, X., Appel, H., Borca, C. H., Le Breton, G., Buchholz, F., Castro, A., Corni, S., Correa, A. A., De Giovannini, U., Delgado, A., Eich, F. G., Flick, J., Gil, G., Gomez, A., Helbig, N., Hübener, H., Jestädt, R., Jornet-Somoza, J., Larsen, A. H., Lebedeva, I. V., Lüders, M., Marques, M. A. L., Ohlmann, S. T., Pipolo, S., Rampp, M., Rozzi, C. A., Strubbe, D. A., Sato, S. A., Schäfer, C., Theophilou, I., Welden, A. & Rubio, A. Octopus, a Computational Framework for Exploring Light-Driven Phenomena and Quantum Dynamics in Extended and Finite Systems. *The Journal of Chemical Physics* **152**, 124119, (2020).

[11] Tancogne-Dejean, N., Oliveira, M. J. T. & Rubio, A. Self-Consistent *DFT+U* Method for Real-Space Time-Dependent Density Functional Theory Calculations. *Phys. Rev. B* **96**, 245133, (2017).

[12] Agapito, L. A., Curtarolo, S. & Buongiorno Nardelli, M. Reformulation of *DFT+U* as a Pseudohybrid Hubbard Density Functional for Accelerated Materials Discovery. *Physical Review X* **5**, 011006, (2015).

[13] Sun, Z., Gutiérrez-Rubio, Á., Basov, D. N. & Fogler, M. M. Hamiltonian Optics of Hyperbolic Polaritons in Nanogranules. *Nano Lett.* **15**, 4455-4460, (2015).
[14] Caldwell, J. D., Kretinin, A. V., Chen, Y., Giannini, V., Fogler, M. M., Francescato, Y., Ellis, C. T., Tischler, J. G., Woods, C. R., Giles, A. J., Hong, M., Watanabe, K., Taniguchi, T., Maier, S. A. & Novoselov, K. S. Sub-Diffractional Volume-Confined Polaritons in the Natural Hyperbolic Material Hexagonal Boron Nitride. *Nat. Commun.* **5**, 5221, (2014).
[15] Zhan, T., Shi, X., Dai, Y., Liu, X. & Zi, J. Transfer Matrix Method for Optics in Graphene Layers. *J. Phys.: Condens. Matter* **25**, 215301, (2013).
[16] Dai, S., Ma, Q., Liu, M. K., Andersen, T., Fei, Z., Goldflam, M. D., Wagner, M., Watanabe, K., Taniguchi, T., Thiemens, M., Keilmann, F., Janssen, G. C. A. M., Zhu, S. E., Jarillo-Herrero, P., Fogler, M. M. & Basov, D. N. Graphene on Hexagonal Boron Nitride as a Tunable Hyperbolic Metamaterial. *Nat. Nanotechnol.* **10**, 682-686, (2015).
[17] Fei, Z., Andreev, G. O., Bao, W., Zhang, L. M., McLeod, A. S., Wang, C., Stewart, M. K., Zhao, Z., Dominguez, G., Thiemens, M., Fogler, M. M., Tauber, M. J., Castro-Neto, A. H., Lau, C. N., Keilmann, F. & Basov, D. N. Infrared Nanoscopy of Dirac Plasmons at the Graphene–SiO_2 Interface. *Nano Lett.* **11**, 4701-4705, (2011).
[18] Reschke, S., Mayr, F., Widmann, S., von Nidda, H.-A. K., Tsurkan, V., Eremin, M. V., Do, S.-H., Choi, K.-Y., Wang, Z. & Loidl, A. Sub-Gap Optical Response in the Kitaev Spin-Liquid Candidate α-$RuCl_3$. *J. Phys.: Condens. Matter* **30**, 475604, (2018).
[19] McLeod, A. S., Kelly, P., Goldflam, M. D., Gainsforth, Z., Westphal, A. J., Dominguez, G., Thiemens, M. H., Fogler, M. M. & Basov, D. N. Model for Quantitative Tip-Enhanced Spectroscopy and the Extraction of Nanoscale-Resolved Optical Constants. *Phys. Rev. B* **90**, 085136, (2014).